Normalized Raman Imaging for Studies of Tissue Physiology of the Kidney

Oh, S.[1,§,±]

Trim, W.V. [1,±]

Diakova, M. [1]

Petrova, K. [1]

Ichimura, T. [2]

Takakura, A. [2]

Karmakar, R. [3]

Nørrelykke, S.F. [3]

Peshkin, L. [1]

Bonventre, J.V. [2]

Kirschner, M. [1,*]

[1] Department of Systems Biology Department, Harvard Medical School, Harvard University. Boston, MA 02115, US.

[2] Renal Division, Brigham and Women's Hospital, Harvard Medical School. Boston, MA 02115, US.

[3] Image Analysis Collaboratory, Harvard Medical School. Boston, MA 02115, US.

[*] Corresponding Author: Marc@hms.harvard.edu.

[§] This author is now affiliated with the Department of Physics and the Department of Cellular Molecular Medicine at the University of California San Diego

[±] These authors contributed equally

Conflicts of interest:

M.K. and S.O. hold a patent for Normalized Raman Imaging (NoRI), US11971357B2, doi: 10.1073/pnas.2117938119.

Author Contributions:

Research design and conception: S.O., W.V.T., T.I., J.V.B., L.P., and M.K.

Primary data collection: S.O., W.V.T., T.I., A.T.

Data analysis and interpretation: S.O., W.V.T., M.D., K.P., T.I., A.T., J.V.B., R.K., S.F.N., L.P., and M.K.

Manuscript writing: S.O., W.V.T., M.D., and M.K.

Acknowledgements:

We would like to thank Dr. ChangHee Lee for his helpful assistance in providing the FiJi script for NoRI channel assembly. We would also like to thank Dr. Xili Liu, Dr. Avik Murkherjee, and Ang Li for their helpful assistance in maintaining the NoRI microscope.

Funding:

This project was supported by the National Institutes of Health/ National Institutes of Aging: R01 AG073341.

Data availability:

All raw code is available at:

https://github.com/kirschnerlab/NoRI

https://github.com/HMS-IAC/nori

https://github.com/MDyakova/NORI_image_segmentation

https://github.com/MDyakova/NORI_feature_extraction

https://hms-iac.github.io/NoRI/

All raw image data are available at Zenodo: [*pending link*].

Abstract:
Histology is the cornerstone of clinical pathology and an essential tool for many areas of medicine. Nevertheless, conventional histological methods, which rely on fixation, embedding, sectioning, and staining, distort cellular architecture, extract key molecules such as lipids, and introduce variability that severely limits reproducibility. Here, we present Normalized Raman Imaging (NoRI), a form of stimulated Raman scattering applied to organ pathology. NoRI enables quantitative, label-free measurements of proteins and lipids at high spatial resolution. NoRI overcomes heterogeneous light scattering from homogeneous tissues by computationally correcting each signal by the combined Raman signals of protein, lipid, and water. This enables quantitative biomass measurements while preserving tissue architecture, thereby facilitating advanced analysis by convolutional neural networks and feature discovery. Here we apply NoRI to the mouse kidney, showing that such imaging can be used to accurately classify tubule types (median F1 [harmonic mean of precision and recall against manual annotation]=0.93), anatomical regions (F1=0.91), and biological sex (F1=0.97) from regions as small as 132.5µm². Under these circumstances, NoRI has revealed novel sex-specific features, including higher cytoplasmic lipid (+6.9mg/mL; p=0.028), nuclear protein (+26.3mg/mL; p<0.001), and capillary protein concentrations (+3.1mg/mL; p<0.001) in female tubules, along with differences in intracellular lipid droplet morphology. In a time-course model of acute kidney injury (AKI), NoRI captured dynamic changes in protein and lipid organization, most pronounced at day 2 post-injury (F1=0.97), and quantified recovery of brush border structures and lipid droplets over 25 days. Lipid measurements were particularly critical for the high accuracy of feature classification and discovery in AKI (F1=1.0). These results establish NoRI as a reproducible, high-resolution, and fully quantitative framework for tissue analysis and feature discovery, far surpassing conventional histology. By preserving tissue architecture and accurately quantifying lipids and proteins, NoRI provides a unique platform to explore and identify unknown biological phenomena in complex tissues, and present as a powerful diagnostic tool for histopathology.

81 **Introduction:**

82 Following the invention of the compound microscope by the Janssens in the late 16th Century, Marcello
83 Malpighi and other physicians pioneered its use for the study of the micro-anatomy of organs(1). By
84 the 19th Century, the modern field of histology had been born. For the succeeding two centuries,
85 microscopy has been at the center of discovery in the biological and medical sciences and for the
86 routine diagnosis of many pathologies, especially cancer. During this time, there were significant
87 improvements in microscopes themselves, but arguably histopathology depended on parallel
88 developments of highly effective means of fixation, embedding, sectioning, and staining. Today's
89 standard approaches to modern histology are closely related to the technologies developed during the
90 golden age of histology in the latter 19th Century(2). Such tools and methods were responsible for
91 some of the greatest discoveries in biology and embryology sciences in the 19th and 20th Centuries.
92 Today, routine clinical pathology still makes use of many of these same approaches, such as
93 formaldehyde as a fixative, paraffin embedding and mechanical sectioning to visualize tissues, and
94 hematoxylin and eosin staining, devised by Nicolaus Wissotsky in 1877. For a long time, it has been
95 appreciated that these means of tissue preparation, though revealing discrete highly contrasting
96 details of cell structure, such as of chromosomes on the mitotic spindle, nevertheless distort more
97 subtle features, which are blurred by the harsh chemical treatments, which also distort cellular
98 structures and extract components of living cells, such as lipids and water-soluble materials. There is
99 also considerable variability in the methods themselves due to variations in dye batches and
100 inconsistent lab practices. Compensating for this inconsistency and distortion is difficult, since no gold
101 standard for comparison exists. Nevertheless, histopathology remains an important part of the
102 armamentarium of both clinical practice and fundamental biology of multicellular animals.

103 To address the limitations of conventional histological approaches, particularly the complete absence
104 of lipid information, we have recently developed a Normalized (stimulated) Raman imaging
105 microscope with associated methods (NoRI)(3, 4). Stimulated Raman scattering microscopy (SRS) had
106 previously been used to quantify cellular materials by Freudiger*, et al.* (5), particularly to reveal lipids

107 but its quantitative limitation by heterogeneous signal attenuation in thick tissue samples limited its
108 applicability(6). To overcome this, Oh*, et al.* (3) developed a normalization process that relied on an
109 additional channel for water. NoRI enabled precise determination of cell protein and lipid mass, at high
110 spatial resolution, in live or fixed tissues by computationally removing light scattering artefacts.
111 Furthermore, it was highly quantitative, a feature important for application of machine learning. With
112 NoRI, chemical composition (namely, protein [CH_3 bonds], lipid [CH_2 bonds], and water) is
113 automatically converted into absolute concentrations(3). This allows for absolute quantification of
114 cellular protein, lipid, and water; such calculations enable extraordinarily accurate cross-comparisons
115 of samples for feature identification. Consequently, NoRI data are unique not only due to their
116 quantitative nature or ability to visualize lipids but also owing to their un-disturbed view of preserved
117 structures. Nevertheless, detailed histopathology has not been explored in complex tissue specimens
118 using NoRI to date.

119 For performing a histopathological analysis using NoRI, we selected the kidney as a candidate organ.
120 The primary functions of the kidney, which Claude Bernard credited with maintaining the "milieu
121 interieur," include: 1. Blood filtration for waste removal, 2. Regulation of total body fluid balance, 3.
122 Metabolic blood acid-base balance, and 4. Regulation of blood pressure. The kidney is also optimal for
123 testing the suitability of NoRI for histopathology owing to its diverse array of distinct cell types
124 comprising the functional unit, or nephron, which has many subunits, as well as the vasculature and
125 interstitium. The kidney is also ideal since it is composed of distinct anatomical regions, including
126 cortex, and outer and inner medulla. Given the critical connection of the kidneys' own physiological
127 function to whole-body physiology, understanding of the microanatomy of the kidney is vital to
128 understanding both its physiology and how it regulates the physiology of the organism. More recently,
129 machine learning methods have attempted to advance kidney histopathology and have offered the
130 prospect of assisted diagnostics for clinicians and pathologists(7-9). Nevertheless, these methods are
131 severely limited by the high variability in the primary image data derived using traditional techniques.
132 As such, deep-level information related to lipids and microarchitecture is lost, and inconsistency is

133 introduced between samples, making the generation of robust models and discovery of generalizable
134 features difficult. Conventional histology, with its limited quantitative capacity and omission of lipids,
135 may never be able to recover subtle, detailed information needed for deep machine learning models
136 that would allow reliable diagnosis of kidney pathology.

137 As a first step to articulate a quantitative and minimally perturbed analysis of kidney microanatomy
138 we utilized quantitative, highly sensitive image data obtained from NoRI microscopy in healthy and
139 diseased mouse kidneys. The consistency of the new microscopic methods enabled an unprecedented
140 application of machine learning, based on absolute quantification of the protein and lipid signals.
141 Application of convolutional neural networks, a powerful form of machine learning, to the NoRI images
142 in the setting of kidney ischemia-reperfusion injury—a model of acute kidney injury—allowed us to
143 explore the potential sensitivity and reproducibility of NoRI for its application to histopathology and
144 feature discovery. These findings show how NoRI represents a unique tool to explore unknown
145 biological phenomena and provide a basis for advanced, automated histopathology in complex live or
146 fixed tissues.

147

148 **Methods and Materials:**

149 *Animals:*

150 Experiments on kidney anatomy and sex differences were performed on C57BL/6 mice, purchased
151 from Charles River Laboratories, which were housed at the Harvard Institutes of Medicine animal
152 facility. Unilateral ischemia reperfusion experiments were performed in male BalbC mice (*described*
153 *below*). Sixteen-week-old mice weighing 23.0–30.6 g (mean: 27.3 g) were used throughout. All animal
154 protocols were approved by the institutional animal care and user committee of the Harvard Medical
155 School.

156

157 Unilateral ischemia reperfusion surgery

158 Studies were performed according to the animal experimental guidelines issued by the Animal Care
159 and Use Committee at Brigham and Women's Hospital, Boston, USA. Male BalbC mice were obtained
160 from Charles River Laboratory and were allowed free access to water and standard mouse chow.
161 Animals were anesthetized with pentobarbital sodium (60mg/kg body weight, intraperitoneally) prior
162 to surgery. Analgia was provided with Ethiqa XR (3.25mg/kg). The mice were placed on a heating pad
163 and body temperatures were maintained between 36.8-37.2ºC throughout the procedure. The kidney
164 was exposed via flank incisions, and unilateral renal ischemia was induced by clamping left renal
165 pedicle with non-traumatic microaneurysm clamps (Roboz, Rockville, MD, USA) for 20 min. The kidneys
166 were returned to the original place, and the incisions were temporarily closed during ischemia. After
167 the clamps were removed, reperfusion of the kidney was visually confirmed. The muscle layer was
168 closed using absorbable sutures and the skin incision was closed using sterile staples. One millilitre of
169 pre-warmed 0.9% normal saline was administered after surgery. The mice were kept on a warm pad
170 until fully recovered, then returned to their cages. Moist food pellets were placed on the bedding for
171 easy access, and animals were monitored twice daily.

172

173 *Kidney resection and fixation:*

174 Following sacrifice, mice were perfused with chilled (4ºC) phosphate buffered saline (PBS) containing
175 10 U/mL sodium heparin. Kidneys were then resected and cut in half, placed into 5 mL 4 %
176 formaldehyde in PBS (Thermo-Fisher Scientific; MA, US), and stored at 4ºC for 24 hours. Following
177 fixation, samples were washed twice with chilled PBS and were stored in PBS containing 0.02 % sodium
178 azide (Sigma-Aldrich; MilliporeSigma. MA, US) at 4ºC for no longer than one-week before analysis.

179

180 *Kidney slices and immunofluorescence processing:*

181 Whole-kidneys were removed from storage and placed into mounting cylinders compatible with the
182 Precisionary ZF-310-0F Compresstome® (Precisionary Instruments LLC.; MA, US) containing 2 %
183 agarose diluted in distilled water (pre-heated to 50ºC) (EZ Pack Agarose™; Benchmark Scientific, Inc.;
184 NJ, US). All buffers used were filtered through a 0.22 µm filter (Corning®; AZ, US) prior to use.
185 Constructs were then kept at 4ºC for 30 minutes to harden the agarose-sample construct. Samples
186 were next placed into the Compresstome® and cut into 120 µm slices at speed setting 4, oscillation
187 setting 2. Individual tissue slices were then placed into ~2 mL chilled PBS (0.02 % sodium azide) within
188 a 12-well plate (VWR International, LLC; NJ, US). Samples were then placed into PBS containing 5 %
189 normal donkey serum (Jackson ImmunoResearch Laboratories Inc.; PA, US) containing 0.02 % sodium
190 azide overnight at 4ºC with gentle rocking. Blocking solution was removed and replaced with PBS
191 containing 0.02 % sodium azide at room temperature with gentle rocking for 20 minutes, repeated
192 three times; these procedures were found to have no influence on the quantification of protein or lipid
193 by NoRI (**Supplementary Fig. 1**).

194 After washing, the wash buffer was replaced with primary antibodies in tandem in PBS containing 0.02
195 % sodium azide for combinations of the following antibodies; Rat anti-mouse endomucin (1: 200) (sc-
196 65495; Santa Cruz Biotechnology, Inc.; CA, US), sheep anti-mouse uromodulin (1: 200) (T0850-02B;
197 USBiological Life Sciences; MA, US), and rabbit anti-mouse aquaporin 2 (1: 200) (29386-1-AP;
198 Proteintech, ChromoTek GmBH; IL, US). Samples were incubated in primary antibody cocktail for 24
199 hours at room temperature with gentle rocking. Primary antibody cocktail solution was then removed
200 and replaced with PBS containing 0.02 % sodium azide for 30 minutes at room temperature with gentle
201 rocking to wash. This wash was repeated 4–6 times.

202 For samples where lotus tetragonolobus lectin (LTL) labelling of brush border was performed following
203 primary antibody incubations, tissue sections were placed into PBS spiked with 10 µM calcium chloride
204 and avidin blocking solution (Vector Laboratories; CA, US) according to manufacturer
205 recommendations for 30 minutes at room temperature with gentle rocking. From this point on, all
206 buffers were spiked with 10 µM calcium chloride according to manufacturer recommendations for
207 samples where LTL was labelled. Samples were then washed at 20-minute intervals for 60 minutes
208 total in PBS containing 0.02 % sodium azide. After washing, samples were placed into PBS (+10 µM
209 calcium chloride) and biotin blocking solution (Vector Laboratories; CA, US) according to manufacturer
210 recommendations for 30 minutes at room temperature with gentle rocking. Samples were then
211 washed at 20-minute intervals for 60 minutes total in PBS containing 0.02 % sodium azide. Samples
212 were then placed into biotinylated LTL antibody solution (1: 250) (B-1325-2; Vector Laboratories, Inc.;
213 CA, US) in PBS (+10 µM calcium chloride) containing 0.02 % sodium azide for 24 hours at room
214 temperature with gentle rocking. Following LTL incubation, samples were washed in PBS (+10 µM
215 calcium chloride) containing 0.02 % sodium azide for 60 minutes 4–6 times at room temperature with
216 gentle rocking. Next, samples were incubated in secondary antibody cocktail solution for 24 hours at
217 room temperature with gentle rocking, in darkness, in PBS (+10 µM calcium chloride) containing 0.02
218 % sodium azide with combinations of the following antibodies; AffiniPure donkey anti-sheep Alexa
219 Fluor® (AF)488 (1: 250) (Jackson ImmunoResearch Laboratories Inc.; PA, US), AffiniPure donkey anti-

220 rabbit AF647 (1: 250) (Jackson ImmunoResearch Laboratories Inc.; PA, US), AffiniPure donkey anti-rat
221 DyeLight™ (DL)405 (1: 250) (Jackson ImmunoResearch Laboratories Inc.; PA, US), and streptavidin
222 AF594 (1: 250) (ThermoFisher Scientific, Inc.; MA, US). Secondary antibody cocktail solution was
223 removed and replaced with PBS (+10 µM calcium chloride) containing 0.02 % sodium azide for 30
224 minutes at room temperature, in darkness, with gentle rocking, repeated 4–6 times.

225 After washing, samples were mounted onto glass slides (Superfrost® Plus VWR MicroSlides; VWR
226 International LLC.; PA, US) with a small amount (~75 µL) of anti-fade mounting solution containing 0.2
227 % propyl-gallate (Sigma-Aldrich; MA, US) diluted in 0.8 % fully deuterated dimethylsulfoxide (DMSO;
228 MilliporeSigma; MA, US) in PBS (+10 µM calcium chloride) containing 0.02 % sodium azide. The
229 deuterated form of DMSO was used so as not to contribute to the NoRI quantitation of the protein
230 methyl groups. Number 1.5 micro cover glass slides (VWR International, LLC.; PA, US) were used to
231 cover samples and slides were sealed using clear nail polish. Samples were stored at 4ºC in darkness
232 in a humidified container until imaging.

233

234 *Fluorescence microscopy and normalized Raman imaging (NoRI):*

235 Microscopy imaging and quantitation was performed on an Olympus FV3000 using Fluoview (Olympus;
236 Tokyo, Japan) and MatLab™ (MathWorks; CA, US). Immunofluorescence imaging was used for cell-type
237 and tubule identification and for identification of markers of cellular stress. The immunocytochemistry
238 was followed by NoRI imaging for protein and lipid quantification. All images were taken using a water
239 immersion 60x 1.2NA objective lens (Evident-Scientific) and an oil immersion 1.4NA condenser lens,
240 where each pixel was equivalent to 414nm for both NoRI and immunofluorescence imaging.

241 Protein and lipid concentrations were calculated from SRS images using NoRI as previously
242 described(3, 4). Briefly, SRS images at 2853 cm^{-1}, 2935 cm^{-1}, and 3420 cm^{-1} bands (corresponding to
243 the methylene- and methyl-groups, and water characteristic vibrational bands, respectively) were

244 acquired from live or fixed cells using a custom-built spectral-focusing femtosecond SRS microscope.
245 This microscope was constructed using synchronized femtosecond pulse lasers for the Pump and
246 Stokes beams. A pair of dense flint (DF) glass rods chirped the pulses. An electro-optical modulator
247 (EOM) modulated the amplitude of the Stokes beam at 20 MHz. A retro-reflector prism mounted on a
248 motorized delay was adjusted to control the overlap of the Pump and Stokes beams. The Pump and
249 Stokes beams, combined by a dichroic mirror (DM), were focused on the sample by the objective lens.
250 Images were acquired by point-scanning using a pair of galvanized mirrors (scan mirror). After passage
251 through the stimulated Raman scattering at the sample plane, the Pump beam was collected by a high
252 numerical aperture condenser lens, selected by a short pass filter (SF), and its intensity was measured
253 by a high-speed photodetector. The three SRS images were spectrally unmixed into protein, lipid, and
254 water components using reference spectra measured from bovine serum albumin solution in water,
255 dioleoyl-phosphocholine solution in per-deuterated methanol, water, and per-deuterated methanol.
256 Unmixed images of protein, lipid, and water components were converted to the absolute
257 concentration by using the sum of the three components as the normalization reference at each pixel.
258 A representative region within each kidney that were imaged is presented in **Supplementary Fig. 2**.

259

260 *Data analysis and image segmentation:*

261 All images were processed by customized codes in Matlab™ (Mathworks) or ImageJ and FiJi (National
262 Institute of Health). NoRI and immunofluorescence images were stitched together using the
263 Grid/Collection stitching plugin for Fiji(10), and stacked into one multi-channel image using a custom
264 macro for FiJi.

265 This study utilized an automated pipeline to quantify protein and lipid concentrations within the
266 cytoplasm of individual kidney tubules. The approach involved three key steps: segmentation,
267 classification, and measurement. A detailed description of this methodology, along with its validation

and application, is also available in Karmakar, Trim, Kirschner and Noerrelykke (11). Segmentation was performed using a combination of classical image processing, deep learning and machine learning techniques, including the Segment Anything Model (SAM) for tubule segmentation(12); with the exception of glomeruli, which were hand-segmented. Post-processing steps, such as morphological operations and expert validation, were applied to refine segmentation accuracy. For comparison with SAM, a YOLOv8-based object segmentation model(13) was also fine-tuned to detect kidney tubules in NoRI images using annotated data derived from the protein and lipid signals. Fine-tuning was conducted on 640×640-pixel image crops, batch size of 16 with 200 epochs (iterations). Early stopping (where learning ends once a model's metrics do not continue to improve further) after 30 epochs was performed. Data augmentation was applied to ensure robustness, using horizontal/vertical flips, random rotations, brightness/contrast adjustments, and affine transformations. All images were normalized using standard ImageNet mean and standard deviation values(14). The model was configured for single-class detection and fine-tuned using the Ultralytics YOLO implementation(13). Tubule classification was performed using Ilastik's(15) object classifier, leveraging immunofluorescence markers (LTL, UMOD, and AQP2) to distinguish tubule types.

Nuclei were segmented using a U-Net model fine-tuned on manually labelled binary masks(16). The input data consisted of 640×640 patches from the protein channel, and corresponding nuclei masks were manually annotated based on visible nuclear morphology. The U-Net architecture followed a standard encoder–decoder design with skip connections and was implemented in PyTorch(17). Fine-tuning was conducted for up to 200 epochs, with a batch size of 8, and learning rate of 0.0001, where an epoch represents one full pass through the dataset, batch size represents the number of samples processed before the model updates its weights, and learning rate represents a step size for adjusting model weights during optimization. For fine-tuning, we used the binary cross-entropy loss and the Adam optimizer(18). Early stopping was applied after 30 epochs without validation improvement. The training data underwent geometric (i.e., rotations, cropping, scaling changes) and photometric (i.e., altered brightness/contrast, noise addition, blurring) augmentations, and all images were normalized

to ImageNet statistics. We chose the model with the best Dice score—where Dice score represents the similarity between two segmented polygons, calculated as twice the intersection area divided by the sum of the areas of the two polygons—as a final model(16). Brush borders were segmented using a U-Net model fine-tuned(16) on manually labelled binary masks. The input data consisted of tubule images of 128×128 patches from the protein channel and lipid channels, and corresponding brush border masks were manually annotated based on visible brush border morphology. The U-Net architecture followed a standard encoder–decoder design with skip connections and was implemented in PyTorch(17). Fine-tuning was conducted using the same parameters as for nuclei. To identify luminal regions within segmented tubules, hierarchical clustering to low-intensity pixels in NoRI images was applied. Pixels were extracted using intensity values below a predefined threshold for each segmented tubule from the maximum projection of all imaging channels. These pixels were clustered using agglomerative hierarchical clustering with a Euclidean distance threshold of 5 pixels. Clusters containing fewer than 75 pixels were discarded to reduce noise. The remaining clusters generated binary masks representing lumen locations within the tissue(19). Nucleoli were segmented using a U-Net model fine-tuned on manually labelled binary masks(16). The input data consisted of nuclei images of 32x32 patches from the protein channel and lipid channels, and corresponding nucleoli masks were manually annotated based on visible morphology. The U-Net architecture followed a standard encoder–decoder design with skip connections and was implemented in PyTorch(17). Fine-tuning was conducted using the same parameters as for nuclei.

Protein and lipid concentrations were quantified by measuring pixel intensities within the cytoplasm, obtained by subtracting the segmented nuclei, nucleoli, lumen, and brush border regions from the tubule mask. Intensity values were converted to concentrations using established conversion factors for protein and lipid. The resulting measurements provided insights into the spatial distribution of these biomolecules across different tubule types.

Feature-based classification, feature extraction, and interpretability analysis

ResNet50 convolutional neural network(20), trained on ImageNet, was used to identify regions of interest in NoRI images. The model's final fully connected layer (where every neuron is connected to every neuron in the neural network's previous layer) was replaced with a new layer corresponding to the number of classes (e.g., cell types, sex, ischemic timepoint) in the dataset. Input images were organized into folders labelled by class and divided into training and validation sets. Image tiles were resized and randomly augmented through horizontal and vertical flips, rotations (0–270°), and random crops. All images underwent normalization using ImageNet's mean and standard deviation. For model fine-tuning, we utilized cross-entropy loss and the Adam optimizer (learning rate = 0.0005) for up to 25 epochs, evaluating performance using accuracy and macro-averaged F1-score (a performance metric on an ascending scale of 0–1 for classification performance calculated as the harmonic mean of precision and recall [$2/(\text{precision}^{-1} + \text{recall}^{-1})$]). The best-performing model weights (i.e., those closest to 1) were saved.

To extract high-level image features (determined by the neural network) and visualize class-specific patterns (i.e., features that determine the class) in NoRI images, fine-tuned ResNet50 models were employed and activations (the output signals produced by a layer of a neural network after it applies its transformation to the input) were retrieved from the penultimate average down sampling layer. Images were transformed using standard normalization and resizing procedures before being passed through the network in evaluation mode. The resulting feature vector was saved and used for dimensionality reduction and visualization with UMAP for each tile. In parallel, Grad-CAM (Gradient-weighted Class Activation Mapping(21)) was applied to layers 2, 3, and 4 of the ResNet architecture to produce class-discriminative heatmaps that highlight image regions most relevant to the model's predictions. These heatmaps were overlaid on grayscale representations of the original inputs to facilitate biological interpretation. UMAP plots and Grad-CAM overlays were generated for validation samples to promote qualitative and quantitative assessment of class differences.

344 Following feature identification by ResNet50, to identify and quantify luminal regions and lipid droplets
345 within segmented tubules and microvasculature regions, hierarchical clustering to low-intensity pixels
346 in NoRI images was applied. Pixels were extracted using intensity values below a predefined threshold
347 for each segmented tubule from the maximum projection of all imaging channels.

348 All code and materials used for image processing can be accessed at: https://github.com/HMS-
349 IAC/nori, https://github.com/MDyakova/NORI_feature_extraction and
350 https://github.com/MDyakova/NORI_image_segmentation. A schematic summary of
351 segmentation and machine learning analysis pipelines is presented in **Supplementary Fig. 3**.
352

353 *Histological preparation and analysis:*

354 A single section of a kidney from five healthy male and five healthy female mice were fixed as described
355 above and were dehydrated, paraffin-embedded, and stained with haematoxylin and eosin by
356 INVIVOVEX LLC. (MA, US). Slides were imaged at 60x magnification on an Olympus slide view VS200.

357

358 *Statistical analysis*:

359 All statistical analyses and graphical representations were performed and produced using MatLab™
360 and GraphPad Prism (MA, US). MatLab scripts are accessible from:
361 https://github.com/kirschnerlab/NoRI. Comparisons between variables, where normally
362 distributed were performed using student's *t*-tests. Where non-normally distributed, Mann-Whitney
363 *U* non-parametric equivalents were used. Cumulative distribution analysis was performed using
364 Kolmogorov-Smirnov tests. For analysis of time-course results, Analysis of Variance (ANOVA) tests
365 were performed, with Bonferroni post-hoc corrections applied. For analysis of ≥3 groups, one-way
366 ANOVA was performed, with Dunn's post-hoc corrections applied. Distribution of raw protein and

lipid concentrations between groups were compared using Kruskal-Wallis tests, with Dunn's post-hoc corrections applied. Effect sizes were estimated using Cohen's *d* calculations throughout. Specific uses of each statistical test are detailed in the respective figure legends. Statistical significance was set at $p \leq 0.05$.

371 **Results:**

372 To establish the potential of NoRI microscopy for exploring tissue biology we first needed to establish
373 its accuracy in measuring proteins and lipids in a well-studied organ under varying conditions. After
374 examining several organs, we chose the intact mouse kidney. We studied the kidney under three
375 physiological or pathophysiological differences: female *versus* male, anatomical variation in the various
376 tissues and cell types in the kidney itself, and the injury and recovery after ischemia-reperfusion injury
377 induced by cessation of renal blood flow followed by reperfusion. At the same time, as we began to
378 appreciate the power of this data set, we experimented with various machine learning methods for
379 analysing NoRI images to measure changes in cells and tissues with known levels of confidence.

380 Samples were imaged by placement between a water immersion 60x 1.2NA objective lens (Evident-
381 Scientific) and an oil immersion 1.4NA condenser lens, where each pixel equated to 414nm for both
382 NoRI and immunofluorescence imaging. A representative kidney section imaged by NoRI is presented
383 in **Fig. 1A**. A single tile (212µm^2) image of NoRI and the corresponding immunofluorescence image is
384 presented in **Fig. 1B**. From such images we derived a mask (i.e., segmented region of interest) of kidney
385 tubules and other structures. A representative tubule structure and a corresponding sub-structure
386 mask is also presented for this same region (**Fig. 1B**). Representative examples of the segmentation of
387 nucleoli are presented in **Supplementary Fig. 4**, and representative images of all image channels and
388 segmentation layers are presented in **Supplementary Fig. 5**. We found that we could fine-tune image
389 models that would parse out tubules, lumen, nuclei, and brush border from the NoRI images, by using
390 a combination of Segment Anything Module (SAM)(12) (for tubules) and YOLO(13) (all remaining sub-
391 structures) fine-tuned against manual segmentation of tubules. Both SAM and YOLO had high mean
392 average precision scores (a single metric that summarizes a model's ability to correctly classify and
393 localize specific objects [e.g., a tubule] across all classes and confidence thresholds, against a gold-
394 standard [e.g., hand-segmented tubules]) for tubule and nuclei segmentation (**Fig. 1C**). We ascertained
395 the variability in cytoplasmic protein and lipid concentrations in proximal tubules (LTL+), distal tubules
396 (UMOD+), and connecting tubule and collecting ducts (AQP2+) in kidney slices from the Midpole

397 region of eight kidneys from four male and four female C57BL/6 mice (**Fig. 1D**). We found that tubule
398 types generally clustered based on their average cytoplasmic protein and lipid concentrations for
399 collecting ducts (Protein: 138.5±19.7 and Lipid: 40.2±13.1mg/mL), proximal tubules (Protein:
400 194.3±18.4 and Lipid: 52.2±9.5mg/mL), and distal tubules (Protein: 170.8±16.1 and Lipid:
401 62.4±10.3mg/mL) (**Fig. 1D**). These results also demonstrated the similarity of tubule cytoplasmic
402 concentrations across animals. Quantification of nuclear protein concentrations for different tubule
403 types and brush border protein/lipid in proximal tubules, and protein and lipid concentrations within
404 the glomeruli is presented in **Fig. 1E**. We observed that nuclei constitute 12.9±4.7% of the tubule area
405 but contained negligible quantities of the lipid within the cell. We also found differences in nuclear
406 protein concentration between tubule types that was statistically significant (134.7±19.3 *versus*
407 166.8±20.3 *versus* 130.7±22.4mg/mL for collecting ducts, proximal tubules, and distal tubules,
408 respectively; $p \leq 0.0001$; **Fig. 1E**). When we took all segmented tubules (not segregated by sub-types),
409 without immunofluorescence channels and processed them through ResNet50, the deep-
410 convolutional neural network (CNN) pipeline, we found NoRI+CNN analyses had the strongest
411 performance for tubule type prediction (mean ± SD F1-score: 0.93 ± 0.04; **Fig. 1G**). By comparison,
412 NoRI protein/lipid data, geometric features (*listed in* **Supplementary Table 1**), or a combination of both
413 were less powerful predictors of tubule type (F1-scores: 0.62±0.10, 0.58±0.13, and 0.67±0.12,
414 respectively; **Fig. 1G**). The impressive UMAP representation of tubule types predicted by NoRI+CNN is
415 presented in **Fig. 1H**.

416 Having found that different tubule types possessed different protein and lipid densities, we asked
417 whether protein and lipid concentration of cells in the kidney vary depending on their anatomical
418 location within the organ. To address this question, we took a section of kidney from three different
419 anatomical regions, namely Rostral pole, Midpole, and Caudal pole portions of both left and right
420 kidneys from two male mice and fine-tuned a ResNet50 pipeline on a sub-section of these images (**Fig.
421 2A**). The Caudal pole region had the highest F1-score for prediction (0.91±0.06; **Fig. 2B**), followed by
422 the Rostral pole (F1-score: 0.79±0.14) and Midpole (F1-score: 0.58: 0.58±0.25) (**Fig. 2B**). We also

423 identified statistically significant differences between all three anatomical regions for cytoplasmic
424 protein, and between all regions, except for Rostral pole and Midpole (p=0.123; **Fig. 2E**), for lipid
425 concentrations across tubules with highest cytoplasmic protein concentrations present in Caudal pole
426 sections (Protein: 158.4±29.5 and Lipid: 49.9±11.5mg/mL), whereas Midpole and Rostral pole were
427 similar across protein and lipid cytoplasmic concentrations ([Rostral pole] Protein: 134.6±21.0 and
428 Lipid: 43.1±9.0mg/mL, and [Midpole] Protein: 136.6±20.8 and Lipid: 42.6±9.0mg/mL)(*ANOVA*: all
429 $p \leq 0.0001$; **Fig. 2D, Fig. 2E** and **Supplementary Fig. 6**). These differences were further supported by
430 medium-to-high effect sizes when comparing distinct tubule types between Rostral pole *versus* Caudal
431 pole (d=0.63–1.21) and Midpole *versus* Caudal pole (d=0.88–1.76), but with less distinction between
432 Rostral pole and Midpole portions (d=0.27–0.99) (**Supplementary Fig. 6**). We also observed a
433 significant downward trend in proximal tubule cytoplasmic protein and lipid concentrations from
434 cortex to medulla in the Midpole region (r^2>0.281, p<0.0001; **Supplementary Fig. 7**). We did not
435 identify any significant differences between regions from left and right kidneys (F1=0.58; *data not*
436 *shown*).

437 We used the ResNet50 pipeline fine-tuned on different kidney regions to identify structural features
438 that might distinguish between regions (representative examples presented in **Fig. 2F**). These analyses
439 identified protein concentrations in spaces between tubules where the tissue microvasculature
440 resides—which we will term, "microvasculature." These represent the microvasculature of the kidney
441 and are a key distinguishing feature between regions, where the highest protein concentration was
442 found in Caudal pole sections (100.5±29.4mg/mL; p<0.0001), while Midpole and Rostral pole were
443 similar (77.2±22.3mg/mL and 78.3±21.2mg/mL, respectively; p>0.999)(**Fig. 2G**). We also found lipid
444 droplet concentration and size were significantly different between regions ($p \leq 0.0001$). Specifically,
445 Caudal pole exhibited highest lipid droplet concentration (84.7±22.9mg/mL), followed by Rostral pole
446 (75.4±22.0mg/mL) and Midpole (66.5±15.6mg/mL)(**Fig. 2H**). Conversely, lipid droplet size was
447 substantially larger in the Midpole (278±418 pixels) compared to Rostral or Caudal pole regions, which
448 were similar, on average (61±193 and 67±98 pixels, respectively) (**Fig. 2I**).

449 After confirming that NoRI combined with CNNs can predict tubule type and anatomical location of
450 tubules in a single kidney, we next turned our focus on examining sexual dimorphism, using four male
451 and four female C57BL/6 mice. We analyzed the cytoplasmic protein and lipid concentrations to
452 characterize broadly the differences between sexes (**Fig. 3A**). Cytoplasmic protein in LTL+ proximal
453 tubules—specialized in resorption of substances back into the bloodstream—was significantly higher
454 in female mice (256.9±6.9mg/mL), on average than for males (245.5±3.2)(p=0.029; **Fig. 3B**).
455 Furthermore, cytoplasmic lipid content was between 6.5–7.3mg/mL more concentrated in female
456 mice across all tubule types analyzed (p≤0.028; **Fig. 3C**). There were no differences between number
457 of tubules between sexes (p≥0.767; **Supplementary Fig. 8**). To probe more deeply into the localization
458 and features underpinning sex differences in mouse kidneys in NoRI images, we fine-tuned image tiles
459 of varying sizes from 40–320 pixels in size (~16.5–132.5µm^2, ranging from a single cell to several
460 tubules per image) to determine what type of input data in the ResNet50 pipeline best captured the
461 differences (**Fig. 3D**). We found a tile size of 320 pixels (132.5µm^2) achieved remarkable F1-scores for
462 predicting the sex of a given tubule, likely due to capturing larger regions of tubules and other
463 structures, though all image tile sizes worked to some degree, with high accuracy to predict the sex of
464 a tubule (average F1-scores: 0.82–0.97; **Fig. 3E**, **Supplementary Fig. 9**). We next explored what were
465 the actual features that ResNet50 that accounted for the sexual dimorphism (**Fig. 3G**). These analyses
466 revealed that the level of nuclear protein and the relative abundance of protein to lipid in the
467 microvasculature region were both significantly greater in females (+26.3mg/mL and +19.5%,
468 respectively; p≤0.001; d=0.82–0.83; **Fig. 3H** and **I**). The concentration of lipid and the size of the lipid
469 droplets were similarly significantly higher in females (+11.65mg/mL and +7.12µm^3, respectively;
470 p≤0.001; d=0.62–0.63; **Fig. 3J** and **K**). We also compared our ability to determine sex in the kidney with
471 conventional histological methods (H&E staining) against our combination of NoRI plus machine
472 learning analyses (**Supplementary Fig. 10**). We found that although sex could be reliably determined
473 from H&E images using ResNet50 (presumably due to the relative importance of protein over lipid as
474 shown by NoRI), the staining inconsistencies, lack of quantitative data, and disruption of tissue

475 architecture in H&E staining failed to register finite/smaller (e.g., sub-cellular-sized) features that could
476 distinguish males from females (i.e., at layers 2 and 3 of the ResNet50 output). Instead, activation maps
477 presented in **Supplementary Fig. 10** highlight sex discrimination was largely focused on macro-
478 structures such as entire tubule bodies, rather than sub-cellular structures/regions. This admittedly
479 unusual metric suggests that NoRI can better distinguish subtle differences in structure than H&E
480 staining and is much more quantitative, allowing for a direct measurement of such structures that are
481 normally lost due to staining variability sample-to-sample, or micro-architectural disturbance from the
482 extensive processing required by conventional histology protocols.

483 Given the success of NoRI in predicting tubule type, anatomical location, and the sex of a tubule simply
484 from structural and chemical composition (protein and lipid mass density) we applied NoRI and
485 convolutional neural networks to better understand kidney dysfunction, in a model of transient
486 unilateral ischemic-reperfusion injury (IRI). This model of acute kidney ischemia, caused by temporary
487 occlusion of the renal artery and vein of one kidney, leaving the other as a contralateral control, is a
488 common model for acute kidney injury (AKI)(22). When due to ischemia, AKI is characterized by oxygen
489 deprivation to inflammation, oxidative stress, renal damage, and recovery which can be "adaptive"
490 with few if any long-term consequences, or "maladaptive" resulting in incomplete repair with tissue
491 scarring/fibrosis (22). As such, this model represents a powerful means of exploring both kidney
492 damage and repair, as commonly occurs in human AKI.

493 In this AKI model, where occlusion occurred for only 20 minutes, we first performed a time course
494 analysis of signs of dysfunction and repair across collecting ducts, distal and proximal tubules. We
495 observed no change in tubule numbers between contralateral control and IRI kidneys at each time
496 point (**Supplementary Fig. 11**). We next analysed the cytoplasmic protein and lipid concentrations of
497 tubule types at each time point post-IRI and found that proximal and distal tubule cytoplasmic lipid
498 concentrations showed changes during the recovery period post-IRI (+6.3mg/ml from day 1 to
499 +8.3mg/mL at day 25 post-IRI, respectively). There were significant reductions in proximal tubule and

500 distal tubule lipid concentrations between groups specifically at day 2 post-IRI (52.9±0.6mg/mL *versus*
501 46.2±0.2mg/mL, and 61.3±2.2mg/mL *versus* 47.0±3.3mg/mL for proximal and distal tubule
502 cytoplasmic lipid concentration in contralateral control *versus* IRI kidneys at day 2 post-IRI,
503 respectively; two-way ANOVA: $p \leq 0.037$; **Supplementary Fig. 12**). We next explored the time course
504 relative to the contralateral control. We took NoRI images from days 1, 2, 5, and 25 post-IRI for both
505 contralateral control and ischemic kidneys and followed the time course of structural changes in kidney
506 dysfunction and repair following the ischemic injury (**Fig. 4A**). In support of the above findings in
507 **Supplementary Fig. 12**, we found the greatest difference between contralateral control and IRI (F1-
508 score: 0.97±0.04) at day 2 post-IRI (**Fig. 4B**). Days 1 and 5 post-IRI displayed similar degrees of
509 separation (F1-scores: 0.77–0.85; **Fig. 4B**). By day 25 post-IRI the distinction between and ischemic
510 kidneys was very much reduced (F1-score: 0.58; **Fig. 4B**). These changing properties were also
511 reflected in the spatial separation between contralateral control and ischemic tubules in **Fig. 4C–E**, but
512 the separation of clusters was not visible at day 25 post-IRI (**Fig. 4F**). We characterized the structural
513 changes imposed by IRI in contralateral control and ischemic kidneys over time to better understand
514 the underlying biological manifestations of AKI. On day 1 post-IRI, there were significant difference in
515 the microvasculature protein (96.4±25.6mg/mL *versus* 113.0±29.7mg/mL for contralateral control
516 *versus* IRI, respectively; $p \leq 0.001$; d=0.61–0.67; **Fig. 4J**), possibly reflective of vascular congestion. On
517 day 2 post-IRI, lipid droplet concentration was significantly lower in ischemic relative to contralateral
518 control kidneys (92.8±22.7mg/mL *versus* 76.8±25.8mg/mL; $p<0.001$), whereas brush border lipid
519 concentration was significantly greater in ischemic kidneys ([median±SEM] 30.7±0.4mg/mL *versus*
520 35.7±0.4mg/mL; $p<0.001$; **Fig. 4K**), however, effect size calculations revealed no effect (d=0.02) at day
521 2 post-IRI (**Fig. 4K**). On day 5 post-IRI, microvasculature protein concentration was also significantly
522 higher in ischemic kidneys (89.0±23.3mg/mL *versus* 110.1±28.0mg/mL for contralateral control *versus*
523 IRI, respectively; $p<0.001$; d=0.84; **Fig. 4L**), while lipid droplet size was significantly (but with small
524 effect), elevated in ischemic kidneys ($p<0.001$; d=0.26; **Fig. 4L**).

525 We anticipated using the contralateral (unligated) kidney as an internal control for the IRI experiment.
526 However, we were aware that the undisturbed contralateral kidney might have suffered an added
527 burden for having to both undertake the function of two kidneys, as well as being exposed to a post-
528 ischemic milieu of stress and damage from response molecules released by the ligated kidney. Thus,
529 we next turned our attention to detecting the effects of IRI on the unligated contralateral control
530 kidney and in ischemic kidney in isolation, over time (**Fig. 5A**). There were, in fact, significant changes
531 over time within both the contralateral control and ischemic kidneys over time (F1-score: 0.77–0.99;
532 **Fig. 5B**), suggesting the contralateral control kidney also exhibits substantial temporal responses post-
533 IRI. Specifically, distinct clustering between days 1 *versus* 2 and days 5 *versus* 25 was apparent in the
534 contralateral control kidney data (**Fig. 5C** and **E**). Indeed, this separation in the contralateral control
535 kidney UMAP clustering was similar to the distinct clustering found between timepoint post-IRI in the
536 ischemic kidneys (**Fig. 5F–H**). Using ResNet50 CNN analyses on the quantitative, undisrupted NoRI
537 images of kidneys we could easily detect changes in both contralateral control and ischemic kidneys
538 post-IRI (*representative images presented in* **Fig. 5I**). We found the concentration of protein within the
539 tubule lumen (representative of a pathological 'protein plug') increased from 30.8±19.3mg/mL to
540 39.9±25.0mg/mL, in contralateral control kidneys, and decreased from 37.1±24.2mg/mL to
541 34.7±22.8mg/mL from day 1 to day 25 post-IRI in ischemic kidneys (**Fig. 5J**), but was not entirely absent
542 by day 25 post-IRI. Lipid droplet concentrations also increased from 88.0±31.2mg/mL to
543 104.3±27.7mg/mL, in contralateral control kidneys, and from 93.8±32.9mg/mL to 94.9±26.4mg/mL
544 from day 1 to day 25 post-IRI in ischemic kidneys (**Fig. 5K**). Finally, we found brush border lipids also
545 increased from 35.4±11.2mg/mL to 43.7±11.0mg/mL, in contralateral control kidneys, and from
546 34.4±11.3mg/mL to 37.6±9.7mg/mL from day 1 to day 25 post-IRI in ischemic kidneys (**Fig. 5M**).
547 However, the comparative lack of brush borders at early time points (pre-day 5 post-IRI) may have
548 caused a skewing of these analyses towards 'less-perturbed' regions that still had brush border present
549 for analysis relative to tubules that entirely lost their brush border and so would be precluded from
550 this analysis. All these features displayed highly significant time effects from day 1 to 25 post-IRI (*two-*

551 *way ANOVA time effect*: $p \leq 0.0001$; **Fig. 5J–M**). Not surprisingly, there were significant interaction
552 effects (all $p \leq 0.0001$) between contralateral control and ischemic kidneys at each timepoint for each
553 of the four anatomical regions quantified in Panels J–M, showing differential effects of ischemia on
554 contralateral control and ischemic kidneys.

555 To understand the power of the quantitative nature of NoRI data when combined with CNNs we
556 examined kidneys from day 2 post-IRI for deeper analysis. We found a considerable improvement in
557 F1-scores (as a measure of accuracy of predicting ischemic from contralateral control kidney images)
558 when we utilized both protein and lipid versus just protein alone (F1=0.84 *versus* 0.99, respectively).
559 This gave us our first sense of the importance of the lipid information, which cannot be studied using
560 conventional histology techniques since lipids are extracted during the embedding procedure. We
561 expanded these analyses by asking how important the absolute quantitative information obtained by
562 NoRI was, compared with less quantitative measurements, for the simple task of distinguishing
563 contralateral control from ischemic kidneys at day 2 post-IRI. To make this comparison we generated
564 non-quantitative NoRI images where samples were normalized on a per-image basis, and protein and
565 lipid were also normalized in isolation from one another (similar to intensity-based histogram
566 adjustments in conventional histology). As expected, there was a reduction in F1-scores from
567 quantitative to non-quantitative data, with a further drop between non-quantitative data when only
568 protein is used compared to protein and lipid together (**Supplementary Fig. 13**).

569 **Discussion**

570 NoRI is a novel microscopy technique that provides a highly quantitative measure of both protein and
571 lipid biomass concentrations at high spatial resolution. As such it represents a potentially powerful
572 new tool for detecting subtle tissue injury or physiological state change. This is the *a priori* argument,
573 but it is only in the setting of real pathology that one can assess the value of any new histopathological
574 method. Hence, our goal in this study was to test NoRI on a realistic problem of tissue physiology; we
575 chose ischemic reperfusion injury in the kidney. We found that in the setting of fully quantitative,
576 spatial information where there was no disturbance to tissue architecture, as provided by NoRI, we
577 were able to characterize, and for the first time, quantitate known features of AKI (e.g., luminal protein
578 plugs and brush border loss), and discover novel features of kidney damage and reparative processes
579 that would not have been possible previously (e.g., lipid droplet concentration heterogeneity, brush
580 border lipid concentrations). Further, we found that precisely because NoRI images are fully
581 quantitative, normalised to a reference calibration on each day of use, and do not require tissue
582 processing, and hence do not cause disruption of tissue architecture, they are fully reproducible. As
583 such, they are the ideal image data for analysis by neural networks. This combination of advanced,
584 unbiased analysis methods, such as with NoRI images, can provide a unique platform to explore and
585 identify previously unknown biological phenomena in the setting of complex tissues, and at the same
586 time to compare the effectiveness of different methods to do so.

587 The standard protocols in histopathology involve fixation, dehydration, generally paraffin embedding,
588 and sectioning. These processes extract lipids, which represent a considerable portion of mammalian
589 cellular biomass. Routine clinical pathology uses an array of techniques, such as stains like hematoxylin
590 and eosin, most recently complemented by immunohistochemistry, usually on microtome-cut,
591 paraffin-embedded tissue slices. Owing to such harsh treatments required by the needs to preserve
592 some tissue architecture and the hardening of tissue that can then be sectioned to thicknesses of less
593 than 10µm, there is only partial preservation of the *in vivo* architecture. These sequential preparation
594 steps are also time-intensive (as much as several days), and the indirect staining/probing methods

exhibit day-to-day variability. As such, while relatively inexpensive, the traditional methods provide an incomplete and imperfect record of tissue architecture. Conversely, the imaging and analytical work, built upon our initial work using NoRI(3), overcomes most of the traditional constraints. Indeed, NoRI is performed in thick (100–500µm, and perhaps up to 1mm) tissue samples that are optically sectioned, rather than mechanically sliced (with an axial resolution of approximately 1.9µm(3)). This allows 3-dimensional high-resolution imaging of cells and organelles and notably does not require tissue processing. It can be performed on formaldehyde-fixed, unfixed or living material(3, 4). It can provide a fully quantitative readout of protein and lipid concentrations, and, by varying the wavelength, can distinguish chemical differences, such as the degree of saturation of lipids and the quantitative levels of cholesterol. With proper protocols in place (i.e., where appropriate machine learning models have been trained prior), imaging and analysis can be performed in <1 hour of tissue presentation. Furthermore, NoRI is fully compatible with immunofluorescence.

As discussed above, NoRI images can be processed quickly (<1 hour) compared to conventional histology (hours-to-days). Once acquired, we have developed protocols for automatically segmenting kidney tubules and substructures (nuclei, nucleoli, brush border, lumen) using two open-access methods—SAM and YOLO v.8—that performed with high precision when compared with laboriously obtained hand-segmented reference data. This unexpected facility can largely be explained by the reproducibility and quantitative nature of NoRI data. Spectrophotometric detection of optimally sectioned material is computationally unmixed to offset any impact of light scattering in complex samples. After trying many computation methods, we settled on an open-access convolutional neural network (ResNet50); it provided a powerful and fast means of high-dimensional analysis of NoRI image. Indeed, we have shown how, with very little input training data (as few as 2–3 input images), we are able to identify three distinct tubule types, anatomical location, biological sex, and disease status of tubules with high confidence. While cytoplasmic protein and lipid concentrations were sufficient to delineate proximal from distal tubules with reasonable confidence, the use of protein, lipid, and geometric data in the ResNet50 pipeline was able to determine different tubule types with

621 near-perfect (against the gold standard of human annotation) certainty. We further discovered the
622 context-specific importance of lipid and protein concentrations during this process. For example, we
623 found that lipids were the most important feature to distinguish contralateral control from ischemic
624 kidneys at day 2 post-IRI, suggesting lipids are central to the early pathology of acute tubular injury.
625 Conversely, protein concentrations were a stronger determinant of predicting the sex of the kidney
626 being analysed, indicating lipid handling within the kidney is more congruent between male and
627 female tubules than is protein. These results importantly show the value of NoRI quantification of both
628 proteins and lipids.

629 Another important characteristic of the quantitative protein and lipid data obtained by NoRI, coupled
630 with the preservation of tissue architecture due to the lack of tissue processing required for NoRI, was
631 the ability to detect small structures of importance in these images. This was made most clear when
632 we applied the same machine learning analysis approaches to both NoRI and H&E sections from the
633 same male and female mice for direct comparison. The value of this finding is in support of the lack of
634 sample processing, and thereby greater preservation of *in situ* tissue architecture with NoRI imaging
635 compared to conventional histology techniques. Using NoRI image data, the neural network models
636 we developed were able to identify, consistently, small and refined structures such as lipid droplets to
637 distinguish males from females. Comparatively, H&E images, analysed using the same approaches,
638 were unable to identify the sex of the kidney from quantitation of such small structures, and instead
639 only identified larger structures, such as tubules, as distinguishing features of male and female kidneys.
640 This side-by-side comparison of NoRI *versus* H&E in the same specimens highlighted that, when
641 combining NoRI with these advanced analysis techniques, we were uniquely positioned to make
642 striking insights into healthy and diseased mouse kidneys.

643

644 **The utility of NoRI in histology and pathology**

645 We chose the kidney as a model system for testing the effectiveness of NoRI, combined with neural
646 networks/machine learning methods for the analyses of tissue histology and/or pathology. The kidney
647 is comprised of highly repeated structures (tubules), distinct anatomical characteristics
648 (cortex/medulla), distinct sub-structures (cytoplasm, brush border, lumens), and a variety of cell types.
649 With these attributes in mind, we addressed three biological questions: the extent and nature of the
650 kidney's anatomical variability, its sexual dimorphism, and anatomical changes in the response to
651 ischemia-reperfusion injury (as a model of Acute Kidney Injury [AKI]).

652 Using NoRI alone we found distinct clustering of cell types solely by their concentration of protein and
653 lipid. This was confirmed by the unique expression of transporters and channels revealed by specific
654 antibodies. The distal tubules, proximal tubules, and collecting ducts are epithelial cells expressing
655 different membrane antigens. Yet, unexpectedly, the cytoplasm of proximal tubules was significantly
656 higher in total protein on average by 24mg/mL and lower in lipid on average by 10mgmL. Collecting
657 ducts were lower in both protein and lipid than either proximal or distal tubules by 32-56mg/mL and
658 12-22mg/mL, on average, respectively. What was also notable from these results was how tightly-
659 regulated the cytoplasmic concentrations of proteins and lipids were within tubule types. The protein
660 concentrations varied on average 17.2mg/mL (9.5%), while the lipid concentrations varied 9.9mg/mL
661 (17.2%). We also found that the nuclear protein content varied between tubule types, with proximal
662 tubules having ~30mg/mL higher protein concentrations than distal tubules or collecting ducts. Before
663 NoRI measurements, such information on the distinctive lipid and protein concentrations in the
664 cytoplasm of kidney tubules has not to our knowledge been previously reported. Differential
665 cytoplasmic lipid content between tubule types may be related to metabolic differences, with proximal
666 tubules biased towards lipid metabolism, evidenced by a greater abundance of PPARα/γ—involved in
667 lipid metabolism—while distal tubules are more glycolytic in nature(23), and therefore less reliant on
668 an intracellular lipid pool. The lower cytoplasmic protein density of proximal tubules may be due to
669 their higher lipid content and enhanced rate of lipid oxidation/turnover. Such observations suggest

670 that quantitative features of protein and lipid density may reflect physiological conditions and be more
671 informative than are morphological phenotypes.

672 Having established that we could determine tubule identify with high confidence, we investigated the
673 anatomical variation of the kidney protein and lipid as related to anatomy. We first examined nephrons
674 in three adjacent anatomical regions—Rostral pole, Midpole, and Caudal pole portions—from cortex
675 to medulla.

676 These three regions were easily distinguishable by NoRI, as exemplified by protein concentration
677 difference in the microvasculature, which ranged 77.2—100.2mg/mL, and was almost 30mg/mL
678 higher in Caudal relative to Rostral or Midpole regions. Likewise, lipid droplet concentrations were
679 considerably different between regions, being highest in Caudal pole sections, whereas lipid droplet
680 size was nearly 3-fold greater in Midpole regions relative to Rostral and Caudal pole sections. These
681 results represent an intriguing insight into the kidney microvasculature. Prior work utilising super-
682 resolution ultrasound imaging in Zucker rats identified the Midpole as the region most dense in
683 microvasculature(24), while we found protein concentration was greatest in the Caudal pole region.
684 This may, of course, represent a species difference that remains to be determined, but may also
685 represent a subtle difference in the microvasculature itself. For instance, should microvasculature be
686 most dense in the Midpole region—as suggested by McDermott*, et al.* (24)—the endothelial cells
687 themselves may have differential cytoplasmic protein concentrations, reflecting the higher Caudal
688 protein concentrations relative to Midpole or Rostral pole regions in the present study.

689 It is well-known that mouse kidneys exhibit some degree of sexual dimorphism, with larger kidneys in
690 males, reflecting differential water and sodium transporter expression(25-27). Human male and
691 female kidneys show different rates of decline in function with age(27), differential endothelial
692 integrity, differential metabolic profiles, and divergent responses to ischemic-reperfusion injury
693 (*summarized in* Steiger*, et al.* (28)). These differences are most pronounced in the cortex and outer
694 stripe of the medulla(29). Consistent with these findings, we were easily able to distinguish male from

695 female kidneys at a structural level with high reproducibility in the NoRI images. On the compositional
696 level, we found cytoplasmic protein content was significantly higher in proximal tubules from female
697 mice (256.9±6.9mg/mL) *versus* males (245.5±3.2mg/mL). By contrast, cytoplasmic lipid was more
698 concentrated across all tubules in female mice (males: 50.2±2.0mg/mL *versus* females:
699 57.1±2.5mg/mL), which could be consistent with the higher resilience to lipid accumulation in female
700 relative to male kidneys(30). This was also supported by another feature: our finding that lipid droplets
701 were, on average, almost 7.2μm^3 larger in female kidneys and brush border lipid concentration was
702 11.65mg/mL more concentrated, on average, in females compared to males. Furthermore, the protein
703 content of the nucleus was also, on average 26.3mg/mL higher in female tubules. It is also known that
704 female brush border transporter expression and function also differ from males, which may be partially
705 androgen-related(30, 31). While the molecular basis underlying molecular differences in the protein
706 content of the nucleus is unknown and the reasons for the much greater lipid density in female brush
707 borders remain uncertain, these findings show that there are several sexual dimorphisms in murine
708 kidneys, which NoRI has been able to provide the first quantitative readouts for. The power of such
709 quantitative measurements by NoRI is significant. Further, we have also shown how, using NoRI
710 coupled with neural network analyses, we can delineate these sexual dimorphisms in regions as small
711 as 16.6μm^2, with ≥85% certainty, emphasizing the pervasive and consistent characteristics of sexual
712 dimorphism in the kidney

713 With this morphological and structural consistency in mind, we applied NoRI to the ischemic-
714 reperfusion injury model of kidney dysfunction and repair that resembles AKI in humans(22, 31, 32).
715 We can replicate the natural event by transiently interrupting the blood supply to one kidney via
716 clamping the renal artery leaving the contralateral kidney unperturbed directly. As discussed further
717 below, we initially assumed the unperturbed kidney would act as a convenient internal contralateral
718 control. The ensuing hypoxia, caused by a transient clamping of the renal artery leads to both acute
719 functional and structural injury to the ligated kidney, and following 25 days from injury, the kidney
720 recovers much of its function and repairs the damage. Histologically, the transient damage results in

721 sporadic patches of injured tubules and necrosis, characterised by protein plugs in the luminal regions
722 and loss of brush borders. During the recovery phase there are morphologically distinct recovering
723 tubules, and seemingly spared healthy tubules(32). It is known that the relative abundance of these
724 damaged and healthy regions depends on the ischemia duration, age, sex, and underlying disease(32).
725 Ischemic injury is known to cause both endothelial and epithelial cell breakdown and swelling(22),
726 which would likely explain the features identified in NoRI images. The accumulation of protein within
727 the inter-tubule regions may perhaps also be reflective of an accumulation of leukocytes and
728 fibroblasts around dead/dying tubules as part of the adaptive response to injury(22, 31, 32), especially
729 in male kidneys(33). We also found day 2 post-injury was hallmarked by differences in lipid droplet
730 concentrations (on average 16mg/mL higher in ischemic relative to contralateral control kidneys) in
731 proximal tubules. Specifically, we observed a steady increase in both protein and lipid within brush
732 border regions by day 25 post-injury relative to day 1 with an average increase of 8.3mg/mL and
733 3.1mg/mL protein, and 16.2mg/mL and 1.1mg/mL lipid concentration in contralateral and ischemic
734 kidneys, respectively. This likely represents the re-establishment of the brush border (more marked in
735 contralateral control than ischemic kidneys).

736 The large changes in lipid amount and distribution suggest that metabolic changes are a central feature
737 of ischemic reperfusion injury. For example, as discussed above, we identified lipid droplet
738 concentrations, and heterogeneity in droplet concentration, as well as brush border lipid
739 concentrations as major determinants of the injury and repair process during this model of AKI. Kidney
740 proximal tubules are heavily reliant on fatty acid oxidation as a primary source of energy production.
741 Defective lipid handling is a hallmark of renal dysfunction and fibrosis(34, 35). It is, therefore,
742 interesting to quantitatively capture distinct changes in lipid droplet concentrations following ischemic
743 injury in both contralateral control and ischemic kidneys, within their spatial context. These
744 observations are greatly facilitated by NoRI given it provides the first quantitative readout of total lipids
745 in AKI, as lipotoxicity is established as a major hallmark of AKI, and a focus of therapeutic
746 developments(35). Lipid droplets are a heterogeneous population of phospholipid monolayer-bound

747 organelles that store neutral lipids, usually for later use by metabolic systems(36, 37). When the lipid
748 supply outweighs utilization, a lipid-storage response is initiated(38). Therefore, it could be expected
749 that ischemic injury, which causes substantial impairments to beta-oxidation capacity in tubules and a
750 switch to anaerobic metabolism(38, 39) would lead to substantial lipid accumulation. The transport of
751 lipid from the blood might be unlinked from the utilization of lipid, which requires oxidative respiration,
752 which has been inhibited by hypoxia. This imbalance would be expected to lead to an accumulation of
753 lipid droplets during transient hypoxia. Though this might seem reasonable, we in fact observe just the
754 opposite, a lower lipid droplet concentration in ischemic kidneys relative to contralateral control
755 kidneys, notably at day 2 post-IRI (92.8±22.7 *versus* 76.8±25.8mg/mL for contralateral control and
756 ischemic kidneys, respectively). This trend persisted to day 25 with lipid droplet concentrations being
757 ~6.5 and 9.4mg/mL lower in ischemic relative to contralateral control kidneys. While the density of
758 lipid droplets may change in response to changes in their biophysical properties and constituent lipids
759 (triglycerides, cholesterol esters, fatty acids), the presence of coalesced regions of lipids following
760 ischemic-reperfusion injury may not represent physiological lipid droplets *per se* and instead may
761 represent pools of lipids within the debris of dead/dying cells. Lipid-droplet membrane protein probing
762 by immunofluorescence may clarify this uncertainty in future work. Thus, if this undirected
763 accumulation of lipids occurs from the remnant lipids from within the dead cells' cytoplasm, then their
764 density could feasibly be less than organelle-bound lipids. Indeed, the observation of significantly large
765 lipid droplets by day 5 post-injury could support this suggestion.

766 An important contribution made by NoRI in the context of the reperfusion-injury model of acute
767 kidney injury used here was the profound influence the injury imparted on the contralateral control
768 kidney over time. Our quantitative histopathology investigations of the responses over time in the
769 contralateral control kidneys identified many features of dysfunction and damage. Notably, we were
770 able to distinctly separate individual time points between days 1 to 25 post-IRI in the contralateral
771 control group, specifically, by performing neural network analysis on NoRI images. Specifically, these
772 models highlighted a gradual increase in luminal protein (i.e., protein plugs) from days 1 to 25, as well

773 as a gradual increase in lipid droplet concentrations, similar to what was observed in the ischemic
774 kidneys. Furthermore, by day 25 post-IRI there was a dramatic increase in brush border protein and
775 lipid concentrations in the contralateral control kidneys, relative to days 1–5 post-IRI, suggestive of a
776 re-establishment of the brush border that was previously reduced in size and density in the
777 contralateral control kidneys. Our observations support prior work that show the structural,
778 transcriptional, and functional dysfunction in the contralateral control kidneys of this model of AKI,
779 but crucially add additional, quantitative data to this body of work.

780 The dysfunction in the contralateral control kidneys can be segregated into short-term (hours/days),
781 medium-term (days/weeks), and long-term (weeks/months) post-injury. In the short-term,
782 contralateral control kidneys exhibit strong transcriptional shifts due to oxidative stress, increased
783 inflammatory cytokines, and metabolic dysfunction(40, 41). Indeed, the contralateral kidney is
784 exposed to the cytokine storm and oxidative stress produced by the ischemic-damaged kidney, which
785 can influence the healthy kidney that is responsible for a greater proportion of the biological function
786 of two kidneys. In this context, we found a notable change in lipid droplet concentrations from
787 ~90mg/mL on day 1 post-IRI to ~105mg/mL by day 25. This provides a quantitative measurement
788 supporting and expanding upon previous reports of downregulated lipid metabolism pathways in the
789 contralateral control kidney within 24-hours of injury(42). Our results represent the first highly
790 sensitive, quantitative measurement of lipid-related effects of ischemic-reperfusion injury, to our
791 knowledge. In the weeks following injury, leukocytes, including activated T-cells, infiltrate both kidneys.
792 This can represent both part of the damage-induced inflammatory program as well as the structural
793 remodelling—in concert with fibroblasts—that occurs within the contralateral kidney as it
794 compensates for the loss of the damaged kidney(43). In this respect, our analyses identified several
795 features of both tubule damage/stress and structural remodelling within the contralateral kidney.
796 These were hallmarked by the gradual increase in luminal protein from ~32mg/mL on day-1 to
797 ~40mg/mL on day-25 post-injury. Likewise, brush borders showed quantitative evidence of either re-
798 establishment post-injury, or increased abundance and/or density of structures by day-25 post-injury,

evidenced by a dramatic increase in protein (from ~125mg/mL to ~140mg/mL) and lipid (from ~36mg/mL to ~44mg/mL) concentrations at day-25 relative to days 1–5 post-injury. Such quantitative tracking of the micro-anatomy of the kidney in the context of AKI constitutes an exciting development of both known features of kidney damage and repair as well as possibly presenting novel features of injury and repair. These data represent initial insights into the power of NoRI as a tool for making novel biological insights into pathological states, as well as being a useful diagnostic tool in histopathology.

Conclusion

We present this first exploration of the potential of NoRI—a fully quantitative normalized form of stimulated Raman spectroscopy that measures protein and lipid content in biological samples—combined with neural network analysis as a tool for feature identification and diagnostics in histopathology. We have shown, using murine kidney as a candidate organ for these investigations, that NoRI is fully capable of analysing complex tissue samples in a way that could be considered superior to conventional histology methods, owing to its comparatively fast turnaround time from sample harvesting to imaging, its ability to analyze samples without the need for destructive or damaging sample processing, and its ability to fully quantify protein and lipids, label-free, at high spatial resolution. Moreover, we have shown how this form of microscopy, due to its absolute (as opposed to relative) quantitation is highly appropriate for analysis by neural networks for feature discovery. Because it is a spectrophotometric absolute measurement, it releases the power of machine learning for unbiased feature discovery, suggesting that it may have strong diagnostic potential in physiology and disease. Finally, due to the reproducibility (both between animals and within tubule types) and the quantitative nature of these data, these advanced analysis approaches require a relatively low level of input data for feature discovery, such that fine-tuned models can be easily derived and applied to related samples. Thus, NoRI could be applied to a vast array of biological questions and disease states to make both novel biological discoveries and facilitate disease diagnostics in the clinical context. Of these questions, both discovery of novel foci, and the early

diagnosis of cancers are fundamental questions that NoRI is well-placed to make advancements in. Likewise, the application of NoRI to the ageing process could add fundamental insights into a poorly understood, biologically relevant phenomenon, especially given the accumulation of lipids in many organs with age, and the fact that senescent cells are characterised by cell swelling and cytoplasmic mass-density uncoupling.

References:

1. B. Bracegirdle, The History of Histology: A Brief Survey of Sources. *History of Science* **15**, 77-101 (1977).
2. O. Bock (2015) A history of the development of histology up to the end of the nineteenth century.
3. S. Oh *et al.*, Protein and lipid mass concentration measurement in tissues by stimulated Raman scattering microscopy. *Proceedings of the National Academy of Sciences* **119**, e2117938119 (2022).
4. X. Liu, S. Oh, M. W. Kirschner, The uniformity and stability of cellular mass density in mammalian cell culture. *Front Cell Dev Biol* **10**, 1017499 (2022).
5. C. W. Freudiger *et al.*, Label-free biomedical imaging with high sensitivity by stimulated Raman scattering microscopy. *Science* **322**, 1857-1861 (2008).
6. A. H. Hill, B. Manifold, D. Fu, Tissue imaging depth limit of stimulated Raman scattering microscopy. *Biomed Opt Express* **11**, 762-774 (2020).
7. N. Suzuki *et al.*, Deep learning-based histopathological assessment of tubulo-interstitial injury in chronic kidney diseases. *Communications Medicine* **5**, 3 (2025).
8. T. T. U. Nguyen *et al.*, Deep-learning model for evaluating histopathology of acute renal tubular injury. *Scientific reports* **14**, 9010 (2024).
9. D. L. Hölscher, R. D. Bülow, M. Strauch, P. Boor, Advances in Computational Nephropathology. *Kidney International* https://doi.org/10.1016/j.kint.2025.06.029 (2025).
10. S. Preibisch, S. Saalfeld, P. Tomancak, Globally optimal stitching of tiled 3D microscopic image acquisitions. *Bioinformatics* **25**, 1463-1465 (2009).
11. R. Karmakar, W. Trim, M. Kirschner, S. Noerrelykke, Kidney Tissue Characterization using Normalized Raman Imaging and Segment-Anything. *bioRxiv* 10.1101/2025.10.09.681509, 2025.2010.2009.681509 (2025).
12. A. Kirillov *et al.* (2023) Segment anything. in *Proceedings of the IEEE/CVF international conference on computer vision*, pp 4015-4026.
13. J. Redmon, S. Divvala, R. Girshick, A. Farhadi (2016) You only look once: Unified, real-time object detection. in *Proceedings of the IEEE conference on computer vision and pattern recognition*, pp 779-788.
14. J. Deng *et al.* (2009) ImageNet: A large-scale hierarchical image database. in *2009 IEEE Conference on Computer Vision and Pattern Recognition*, pp 248-255.
15. S. Berg *et al.*, ilastik: interactive machine learning for (bio)image analysis. *Nature Methods* **16**, 1226-1232 (2019).
16. T. Falk *et al.*, U-Net: deep learning for cell counting, detection, and morphometry. *Nature Methods* **16**, 67-70 (2019).
17. J. Ansel *et al.* (2024) PyTorch 2: Faster Machine Learning Through Dynamic Python Bytecode Transformation and Graph Compilation. in *Proceedings of the 29th ACM International Conference on Architectural Support for Programming Languages and Operating Systems, Volume 2* (Association for Computing Machinery, La Jolla, CA, USA), pp 929–947.
18. D. P. Kingma, J. Ba, Adam: A Method for Stochastic Optimization. *CoRR* **abs/1412.6980** (2014).
19. J. Nunez-Iglesias, R. Kennedy, T. Parag, J. Shi, D. B. Chklovskii, Machine learning of hierarchical clustering to segment 2D and 3D images. *PloS one* **8**, e71715 (2013).

20. K. He, X. Zhang, S. Ren, J. Sun (2016) Deep residual learning for image recognition. in *Proceedings of the IEEE conference on computer vision and pattern recognition*, pp 770-778.
21. R. R. Selvaraju *et al.*, Grad-CAM: Visual Explanations from Deep Networks via Gradient-Based Localization. *International Journal of Computer Vision* **128**, 336-359 (2020).
22. J. V. Bonventre, L. Yang, Cellular pathophysiology of ischemic acute kidney injury. *The Journal of clinical investigation* **121**, 4210-4221 (2011).
23. Z. Lyu *et al.*, PPARγ maintains the metabolic heterogeneity and homeostasis of renal tubules. *eBioMedicine* **38**, 178-190 (2018).
24. A. McDermott *et al.*, Analysing the Renal Vasculature Using Super-Resolution Ultrasound Imaging: Considerations for Clinical and Research Applications. *Diagnostics (Basel)* **15** (2025).
25. S. A. Kalucki *et al.*, Reference values and sex differences in absolute and relative kidney size. A Swiss autopsy study. *BMC Nephrology* **21**, 289 (2020).
26. A. A. McDonough, A. N. Harris, L. Xiong, A. T. Layton, Sex differences in renal transporters: assessment and functional consequences. *Nature Reviews Nephrology* **20**, 21-36 (2024).
27. T. Melsom *et al.*, Sex Differences in Age-Related Loss of Kidney Function. *J Am Soc Nephrol* **33**, 1891-1902 (2022).
28. S. Steiger *et al.*, Sex dimorphism in kidney health and disease: mechanistic insights and clinical implication. *Kidney International* **107**, 51-67 (2025).
29. S. Chen *et al.*, Multi-omic and spatial analysis of mouse kidneys highlights sex-specific differences in gene regulation across the lifespan. *Nature Genetics* **57**, 1213-1227 (2025).
30. F. Juszczak *et al.*, Sex differences in obesity-induced renal lipid accumulation revealed by lipidomics: a role of adiponectin/AMPK axis. *Biol Sex Differ* **14**, 63 (2023).
31. L. C. Veiras *et al.*, Sexual Dimorphic Pattern of Renal Transporters and Electrolyte Homeostasis. *J Am Soc Nephrol* **28**, 3504-3517 (2017).
32. E. E. Hesketh *et al.*, Renal ischaemia reperfusion injury: a mouse model of injury and regeneration. *J Vis Exp* 10.3791/51816 (2014).
33. K. M. Park, J. I. Kim, Y. Ahn, A. J. Bonventre, J. V. Bonventre, Testosterone is responsible for enhanced susceptibility of males to ischemic renal injury. *The Journal of biological chemistry* **279**, 52282-52292 (2004).
34. L. E. Lee, T. Doke, D. Mukhi, K. Susztak, The key role of altered tubule cell lipid metabolism in kidney disease development. *Kidney International* **106**, 24-34 (2024).
35. A. A. Otunla, K. Shanmugarajah, A. H. Davies, J. Shalhoub, Lipotoxicity and immunometabolism in ischemic acute kidney injury: current perspectives and future directions. *Frontiers in Pharmacology* **Volume 15 - 2024** (2024).
36. N. Mejhert *et al.*, The Lipid Droplet Knowledge Portal: A resource for systematic analyses of lipid droplet biology. *Developmental Cell* **57**, 387-397.e384 (2022).
37. A. E. Ventura *et al.*, Cell lipid droplet heterogeneity and altered biophysical properties induced by cell stress and metabolic imbalance. *Biochimica et Biophysica Acta (BBA) - Molecular and Cell Biology of Lipids* **1868**, 159347 (2023).
38. N. Mejhert *et al.*, Partitioning of MLX-Family Transcription Factors to Lipid Droplets Regulates Metabolic Gene Expression. *Mol Cell* **77**, 1251-1264.e1259 (2020).

39. P. Erpicum, P. Rowart, J.-O. Defraigne, J.-M. Krzesinski, F. Jouret, What we need to know about lipid-associated injury in case of renal ischemia-reperfusion. *American Journal of Physiology-Renal Physiology* **315**, F1714-F1719 (2018).
40. H. Fatemikia, F. Ketabchi, Z. Karimi, S. M. S. Moosavi, Distant effects of unilateral renal ischemia/reperfusion on contralateral kidney but not lung in rats: the roles of ROS and iNOS. *Canadian Journal of Physiology and Pharmacology* **94**, 477-487 (2015).
41. T. Möckel, S. Boegel, A. Schwarting, Transcriptome analysis of renal ischemia/reperfusion (I/R) injury in BAFF and BAFF-R deficient mice. *PloS one* **18**, e0291619 (2023).
42. A. M. Scantlebery *et al.*, The dysregulation of metabolic pathways and induction of the pentose phosphate pathway in renal ischaemia-reperfusion injury. *The Journal of pathology* **253**, 404-414 (2021).
43. D. P. Basile, E. C. Leonard, D. Tonade, J. L. Friedrich, S. Goenka, Distinct effects on long-term function of injured and contralateral kidneys following unilateral renal ischemia-reperfusion. *Am J Physiol Renal Physiol* **302**, F625-635 (2012).

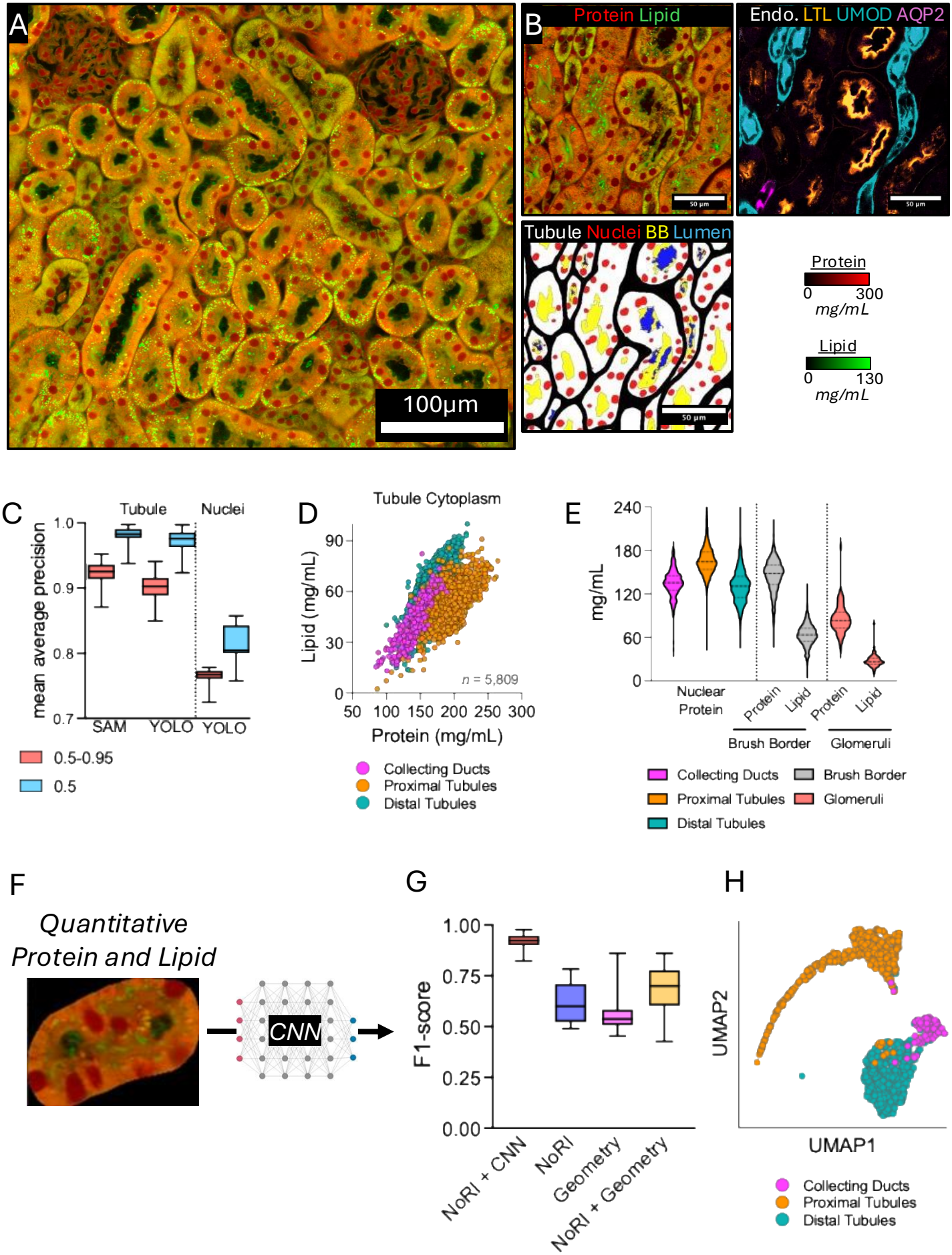
A
100µm
B
Protein Lipid
Endo. LTL UMOD AQP2
Tubule Nuclei BB Lumen
50 µm
Protein
0 300
mg/mL
Lipid
0 130
mg/mL
C
Tubule
Nuclei
mean average precision
1.0
0.9
0.8
0.7
SAM
YOLO
YOLO
0.5-0.95
0.5
D
Tubule Cytoplasm
Lipid (mg/mL)
90
60
30
0
50 100 150 200 250 300
Protein (mg/mL)
n = 5,809
Collecting Ducts
Proximal Tubules
Distal Tubules
E
mg/mL
240
180
120
60
0
Nuclear Protein
Protein
Lipid
Protein
Lipid
Brush Border
Glomeruli
Collecting Ducts
Proximal Tubules
Distal Tubules
Brush Border
Glomeruli
F
Quantitative Protein and Lipid
CNN
G
F1-score
1.00
0.75
0.50
0.25
0.00
NoRI + CNN
NoRI
Geometry
NoRI + Geometry
H
UMAP2
UMAP1
Collecting Ducts
Proximal Tubules
Distal Tubules

Figure 1. Overview of the use of NoRI and CNNs in mouse kidneys

A, Representative NoRI image of mouse kidney. Quantitative readouts of Protein (Red) and Lipid (Green) are displayed. Scale bars representing quantitative protein and lipid signals are presented to the right.

B, Sub-section of mouse kidney simultaneously imaged by NoRI (Left) and immunofluorescence (Right) for tubule type identification, with a representative segmentation mask (Bottom) for tubules, nuclei, brush border, and lumen.

C, Box-whisker plots of mean average precision (0.5 and 0.5-0.95) scores for tubules and nuclei using SAM and YOLOv.8. Scores are relative to hand segmentation of the same structures. Boxes represent median with $25^{th}/75^{th}$ percentiles. Whiskers represent min-to-max values.

D, Scatter plot of cytoplasmic protein and lipid content on a per-tubule basis for two (1x5 mm) kidney sections representing cortex to medulla from the Midpole portion of the left kidney. Color labels for tubule types were assigned according to immunofluorescence staining.

E, Violin plot of nuclear protein, brush border, and glomeruli protein and lipid content on a per-tubule basis for tubules also displayed in Panel D. Data represent a total of 1,662 tubules. Violins are presented with median (dashed line) and $25^{th}/75^{th}$ percentiles (dotted lines).

F, Representative NoRI image of a single tubule analysed by ResNet50 for tubule-type identification by NoRI images without immunofluorescence.

G, Box-whisker plots of F1-scores for tubules input into ResNet50 for tubule prediction. Comparisons between ResNet50 (CNN + NoRI) analyses is presented against each module within the data, including protein and lipid data alone (NoRI), Geometry only, and NoRI+Geometry. Boxes represent median with $25^{th}/75^{th}$ percentiles. Whiskers represent min-to-max values.

H, UMAP plot of tubules clustered by ResNet50. Color coding represents tubule identification assigned by immunofluorescence. Each datapoint represents an individual tubule.

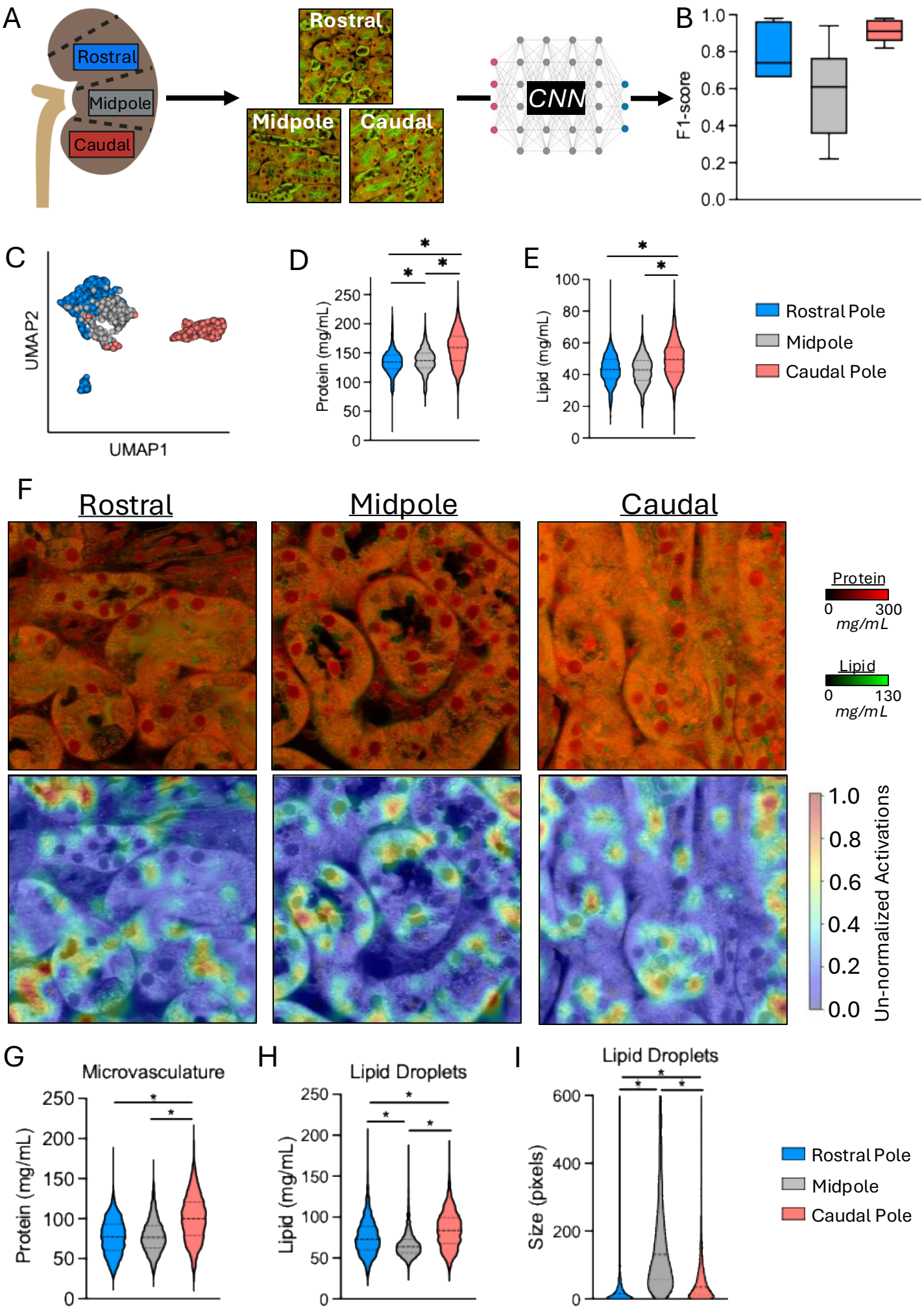
A
Rostral
Midpole
Caudal
Rostral
Midpole
Caudal
CNN
B
F1-score
1.0
0.8
0.6
0.4
0.2
0.0
C
UMAP2
UMAP1
D
Protein (mg/mL)
250
200
150
100
50
0
E
Lipid (mg/mL)
100
80
60
40
20
0
Rostral Pole
Midpole
Caudal Pole
F
Rostral
Midpole
Caudal
Protein
0
300
mg/mL
Lipid
0
130
mg/mL
1.0
0.8
0.6
0.4
0.2
0.0
Un-normalized Activations
G
Microvasculature
Protein (mg/mL)
H
Lipid Droplets
Lipid (mg/mL)
I
Lipid Droplets
Size (pixels)
600
400
200
0
Rostral Pole
Midpole
Caudal Pole

Figure 2. Exploration of kidney anatomy by NoRI.

A, Schematic of experimental design, wherein 2-3 kidney sections from three distinct anatomical regions were imaged by NoRI and input into ResNet50.

B, Box-whisker plots of F1-scores for anatomical region prediction on a per-tubule basis. Boxes represent median with $25^{th}/75^{th}$ percentiles. Whiskers represent min-to-max values.

C, UMAP plot of tubules color coded by anatomical region predicted by ResNet50. Each datapoint represents an individual tubule.

D, Violin plots of tubule cytoplasmic protein content measured by NoRI, split by anatomical region. Violins are presented with median (dashed line) and $25^{th}/75^{th}$ percentiles (dotted lines).

E, Violin plots of tubule cytoplasmic lipid content measured by NoRI, split by anatomical region. Violins are presented with median (dashed line) and $25^{th}/75^{th}$ percentiles (dotted lines).

F, Representative NoRI images from each anatomical region with heatmap of features defining each region identified by ResNet50.

G, Violin plot of microvasculature protein concentration identified by ResNet50 between anatomical regions. Violins are presented with median (dashed line) and $25^{th}/75^{th}$ percentiles (dotted lines).

H, Violin plot of lipid droplet lipid concentration identified by ResNet50 between anatomical regions. Violins are presented with median (dashed line) and $25^{th}/75^{th}$ percentiles (dotted lines).

I, Violin plot of lipid droplet size (in pixels) identified by ResNet50 between anatomical regions. Violins are presented with median (dashed line) and $25^{th}/75^{th}$ percentiles (dotted lines).

Statistical comparisons in Panels D, E, G–I were performed using Kruskal-Wallis tests with Dunn's post-hoc corrections applied.

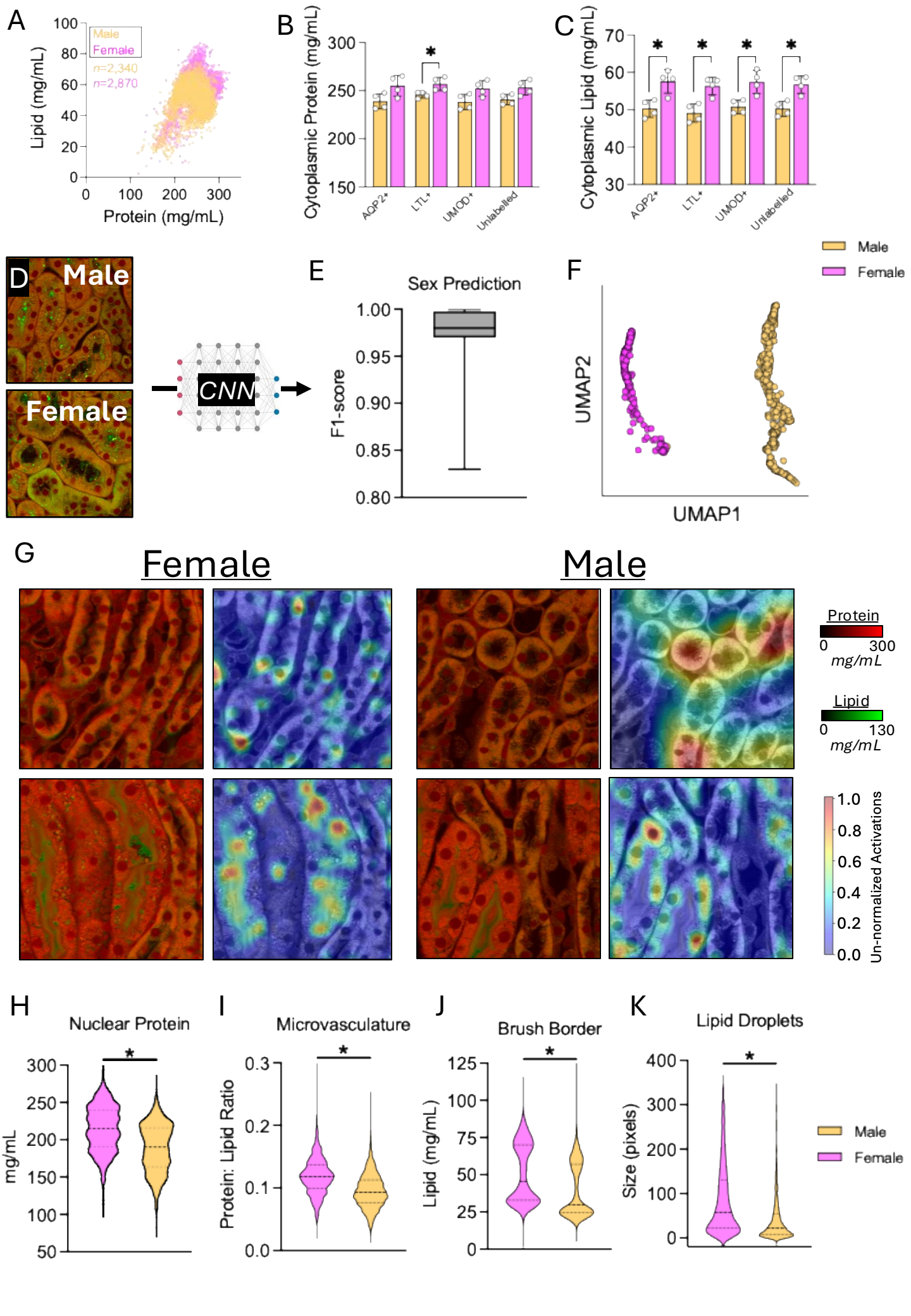
A
Male
Female
n=2,340
n=2,870
Lipid (mg/mL)
Protein (mg/mL)
B
Cytoplasmic Protein (mg/mL)
AQP2+
LTL+
UMOD+
Unlabelled
C
Cytoplasmic Lipid (mg/mL)
Male
Female
D
Male
Female
CNN
E
Sex Prediction
F1-score
F
UMAP2
UMAP1
G
Female
Male
Protein
mg/mL
Lipid
mg/mL
Un-normalized Activations
H
Nuclear Protein
mg/mL
I
Microvasculature
Protein: Lipid Ratio
J
Brush Border
Lipid (mg/mL)
K
Lipid Droplets
Size (pixels)
Male
Female

Figure 3. Exploration of kidney sex differences by NoRI.

A, Scatter plot of tubule cytoplasmic protein and lipid content measured by NoRI in male and female kidneys (*n* = 4 mice per group). Each datapoint represents an individual tubule.

B, Bar graph of cytoplasmic protein content, split by tubule type, measured by NoRI in male and female kidneys. Each datapoint represents the mean value across all tubules for an individual mouse.

C, Bar graph of cytoplasmic lipid content, split by tubule type, measured by NoRI in male and female kidneys. Each datapoint represents the mean value across all tubules for an individual mouse.

D, Representative NoRI images from male and female mouse kidneys input into ResNet50 for sex prediction on a per-tubule basis.

E, Box-whisker plots of F1-scores for sex prediction on a per-tubule basis from NoRI images. Boxes represent median with $25^{th}/75^{th}$ percentiles. Whiskers represent min-to-max values.

F, UMAP plot of tubules color coded by sex and tubule type predicted by ResNet50. Each datapoint represents an individual tubule.

G, Heatmap figures of female and male kidneys imaged by NoRI representing regions discriminating male from female kidneys according to ResNet50.

H, Violin plot of nuclear protein concentrations identified by ResNet50 between sexes. Violins are presented with median (dashed line) and $25^{th}/75^{th}$ percentiles (dotted lines).

I, Violin plot of microvasculature protein: lipid ratio identified by ResNet50 between sexes. Violins are presented with median (dashed line) and $25^{th}/75^{th}$ percentiles (dotted lines).

J, Violin plot of brush border lipid concentration identified by ResNet50 between sexes. Violins are presented with median (dashed line) and $25^{th}/75^{th}$ percentiles (dotted lines).

K, Violin plot of lipid droplet size (in pixels) identified by ResNet50 between sexes. Violins are presented with median (dashed line) and $25^{th}/75^{th}$ percentiles (dotted lines).

Statistical comparisons in Panels B and C were performed using Kruskal-Wallis tests with Dunn's post-hoc corrections applied. Data in Panels H–K were analysed by Kolmogorov-Smirnov tests.

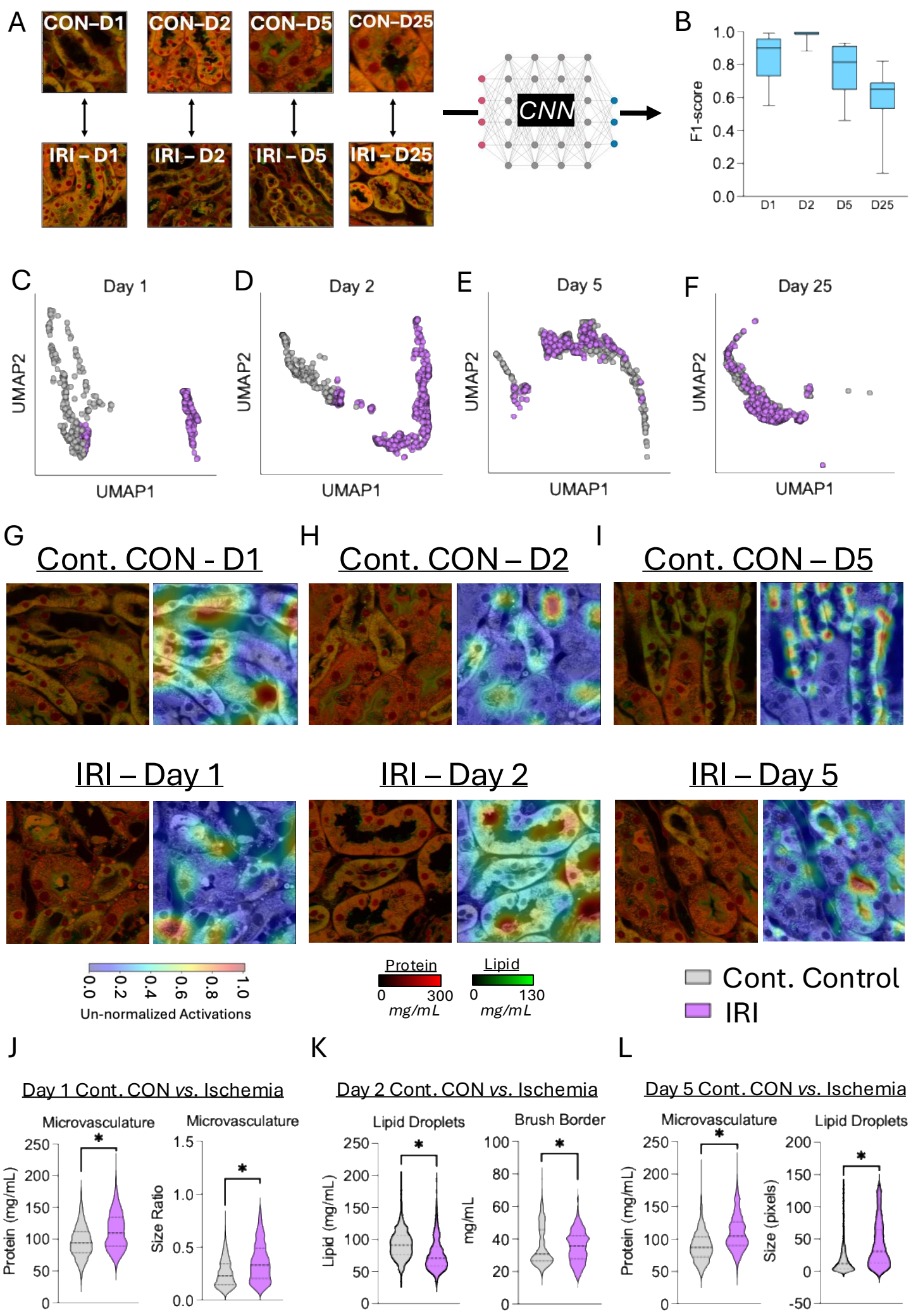
A
CON–D1
CON–D2
CON–D5
CON–D25
IRI – D1
IRI – D2
IRI – D5
IRI – D25
CNN
B
F1-score
1.0
0.8
0.6
0.4
0.2
0.0
D1
D2
D5
D25
C
Day 1
D
Day 2
E
Day 5
F
Day 25
UMAP2
UMAP1
G
Cont. CON - D1
H
Cont. CON – D2
I
Cont. CON – D5
IRI – Day 1
IRI – Day 2
IRI – Day 5
0.0
0.2
0.4
0.6
0.8
1.0
Un-normalized Activations
Protein
0
300
mg/mL
Lipid
0
130
mg/mL
Cont. Control
IRI
J
Day 1 Cont. CON vs. Ischemia
Microvasculature
Protein (mg/mL)
Microvasculature
Size Ratio
K
Day 2 Cont. CON vs. Ischemia
Lipid Droplets
Lipid (mg/mL)
Brush Border
mg/mL
L
Day 5 Cont. CON vs. Ischemia
Microvasculature
Protein (mg/mL)
Lipid Droplets
Size (pixels)

Figure 4. Exploration of the time-course effects of kidney ischemic reperfusion injury by NoRI

A, Representative NoRI images from each time point following ischemic reperfusion injury in both contralateral control (CON) and ischemic (IRI) kidneys input into ResNet50.

B, Box-whisker plots of F1-scores for prediction of contralateral control vs IRI kidneys at each time point post-injury by ResNet50. Boxes represent median with $25^{th}/75^{th}$ percentiles. Whiskers represent min-to-max values.

C, UMAP plot of Cont. CON (contralateral control) (Grey) and IRI (Purple) tubules at day 1 post-injury predicted by ResNet50. Each datapoint represents an individual tubule.

D, UMAP plot of Cont. CON (contralateral control) (Grey) and IRI (Purple) tubules at day 2 post-injury predicted by ResNet50. Each datapoint represents an individual tubule.

E, UMAP plot of Cont. CON (contralateral control) (Grey) and IRI (Purple) tubules at day 5 post-injury predicted by ResNet50. Each datapoint represents an individual tubule.

F, UMAP plot of Cont. CON (contralateral control) (Grey) and IRI (Purple) tubules at day 25 post-injury predicted by ResNet50. Each datapoint represents an individual tubule.

G, Representative NoRI images from Cont. CON (contralateral control) and IRI kidneys at day 1 post-injury with adjacent heatmap of features defining CON from IRI identified by ResNet50.

H, Representative NoRI images from Cont. CON (contralateral control) and IRI kidneys at day 2 post-injury with adjacent heatmap of features defining CON from IRI identified by ResNet50.

I, Representative NoRI images from Cont. CON (contralateral control) and IRI kidneys at day 5 post-injury with adjacent heatmap of features defining Cont. CON (contralateral control) from IRI identified by ResNet50.

J, Violin plots of microvasculature protein content and size measured by NoRI between Cont. CON (contralateral control) and IRI on day 1 post-injury. Violins are presented with median (dashed line) and $25^{th}/75^{th}$ percentiles (dotted lines).

K, Violin plots of lipid droplet concentration and brush border lipid concentration measured by NoRI between Cont. CON (contralateral control) and IRI on day 2 post-injury. Violins are presented with median (dashed line) and $25^{th}/75^{th}$ percentiles (dotted lines).

L, Violin plots of microvasculature protein concentration and lipid droplet size measured by NoRI between Cont. CON (contralateral control) and IRI on day 5 post-injury. Violins are presented with median (dashed line) and $25^{th}/75^{th}$ percentiles (dotted lines).

Data in Panels J–L were analysed by Kolmogorov-Smirnov tests.

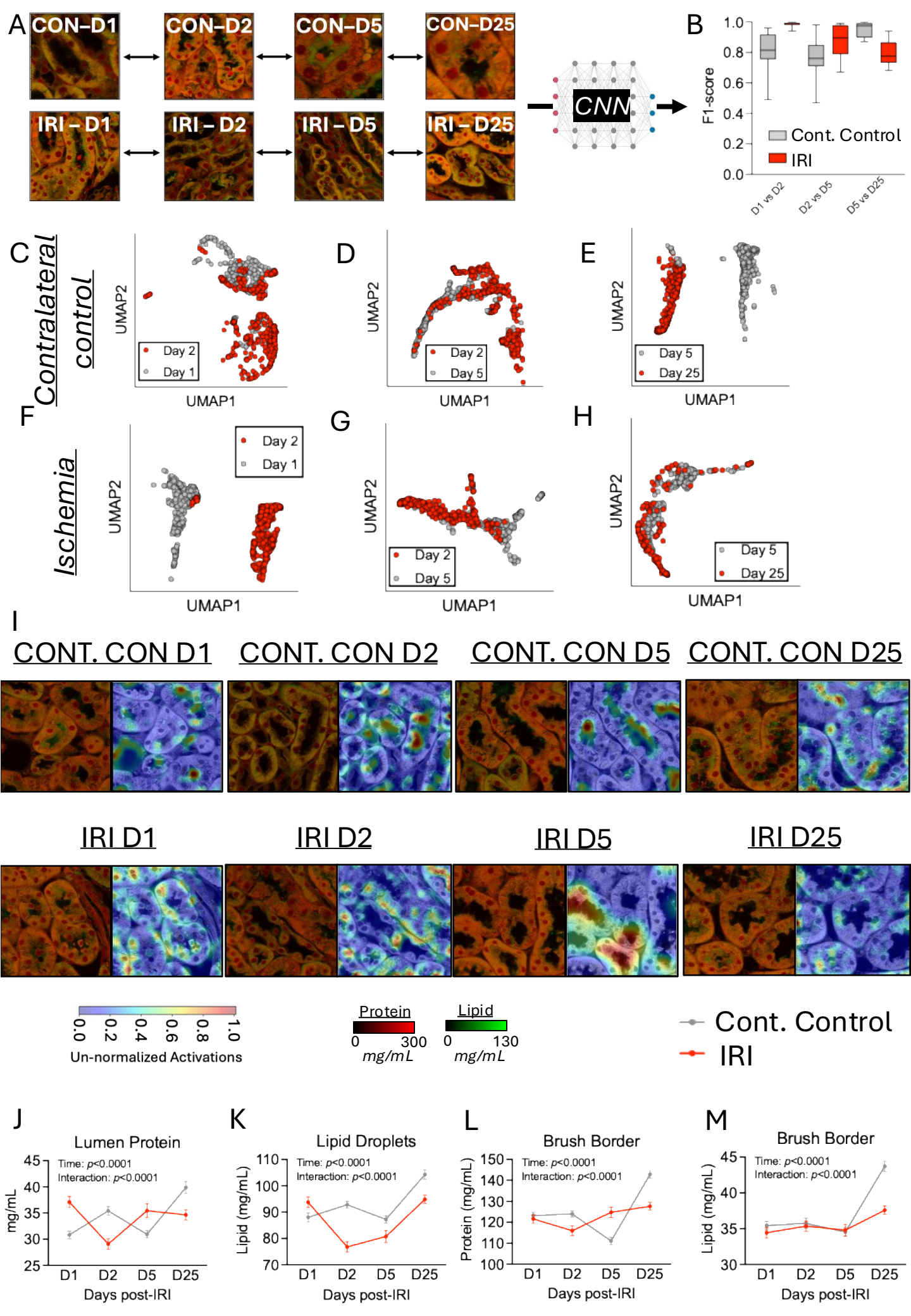
A
CON–D1
CON–D2
CON–D5
CON–D25
IRI – D1
IRI – D2
IRI – D5
IRI – D25
CNN
B
F1-score
Cont. Control
IRI
D1 vs D2
D2 vs D5
D5 vs D25
C
D
E
F
G
H
Contralateral control
Ischemia
UMAP1
UMAP2
Day 2
Day 1
Day 5
Day 25
I
CONT. CON D1
CONT. CON D2
CONT. CON D5
CONT. CON D25
IRI D1
IRI D2
IRI D5
IRI D25
Un-normalized Activations
Protein
Lipid
mg/mL
Cont. Control
IRI
J
Lumen Protein
K
Lipid Droplets
L
Brush Border
M
Brush Border
Time: p<0.0001
Interaction: p<0.0001
mg/mL
Lipid (mg/mL)
Protein (mg/mL)
Days post-IRI

Figure 5. Time course analysis of the effects of ischemic reperfusion injury within contralateral control and IRI kidneys.

A, Representative NoRI images from each time point following ischemic reperfusion injury in both contralateral control (CON) and ischemic (IRI) kidneys input into ResNet50.

B, Box-whisker plots of F1-scores for prediction of the time point post-injury for Cont. Control (contralateral control) and IRI by ResNet50. Boxes represent median with $25^{th}/75^{th}$ percentiles. Whiskers represent min-to-max values.

C, UMAP plot of day 1 (grey) and day 2 (red) tubules for CON kidneys post-injury predicted by ResNet50. Each datapoint represents an individual tubule.

D, UMAP plot of day 2 (grey) and day 5 (red) tubules for CON kidneys post-injury predicted by ResNet50. Each datapoint represents an individual tubule.

E, UMAP plot of day 5 (grey) and day 25 (red) tubules for CON kidneys post-injury predicted by ResNet50. Each datapoint represents an individual tubule.

F, UMAP plot of day 1 (grey) and day 2 (red) tubules for IRI kidneys post-injury predicted by ResNet50. Each datapoint represents an individual tubule.

G, UMAP plot of day 2 (grey) and day 5 (red) tubules for IRI kidneys post-injury predicted by ResNet50. Each datapoint represents an individual tubule.

H, UMAP plot of day 5 (grey) and day 25 (red) tubules for IRI kidneys post-injury predicted by ResNet50. Each datapoint represents an individual tubule.

I, Representative NoRI images from CONT. CON (contralateral control) and IRI kidneys at days 1, 2, 5, and 25 post-injury with adjacent heatmap of features defining each time point, within CON and IRI kidneys identified by ResNet50.

J, Line graph of lumen protein concentration measured by NoRI at each time point post-injury for CONT. CON (contralateral control) (grey) and IRI (red). The mean value for each group at a given time point post-injury is presented, with error bars representing SEM.

K, Line graph of lipid droplet concentration measured by NoRI at each time point post-injury for CONT. CON (contralateral control) (grey) and IRI (red). The mean value for each group at a given time point post-injury is presented, with error bars representing SEM.

L, Line graph of brush border protein concentration measured by NoRI at each time point post-injury for CONT. CON (contralateral control) (grey) and IRI (red). The mean value for each group at a given time point post-injury is presented, with error bars representing SEM.

M, Line graph of brush border lipid concentration measured by NoRI at each time point post-injury for CONT. CON (contralateral control) (grey) and IRI (red). The mean value for each group at a given time point post-injury is presented, with error bars representing SEM.

Data in Panels J-M were analysed by two-way repeated measured ANOVA with Bonferroni post-hoc corrections applied.